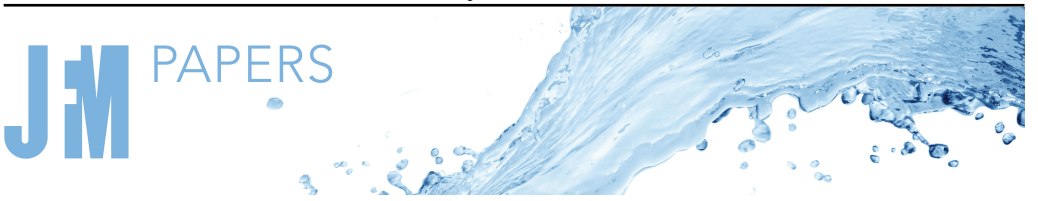
J. Fluid Mech. (2026), *vol.* 1046, A62, doi:10.1017/jfm.2026.12176



Transversely segregated longitudinal stripes in bidisperse granular flows

Amber P. Pearse[1], **Chris G. Johnson**[1] **and J.M.N.T. Gray**[1]

[1]Department of Mathematics and Manchester Centre for Nonlinear Dynamics, University of Manchester, Oxford Road, Manchester M13 9PL, UK

Corresponding author: J.M.N.T. Gray, nico.gray@manchester.ac.uk

(Received 3 March 2026 UTC; revised 4 September 2026 UTC; accepted 8 September 2026 UTC)

Transversely segregated longitudinal flow bands, or stripes, can form in rapid thin dense granular flows due to the formation of a series of counter-rotating secondary vortices whose axes of rotation are aligned with the flow direction (Pearse *et al.* 2026 *J. Fluid Mech.* **1032**, A4). The formation of the secondary vortices is still a subject of active research, but it is likely due to a combination of dilatation and second-normal-stress differences. This paper assumes the existence of the secondary flow and investigates how large and small particles are able to segregate to form stable compositional stripes. In the absence of diffusion, the secondary flow rotates the sharp interface between large particles (above) and small particles (below), around to the vertical, where it breaks to form a series of pure large- and pure small-particle bands that extend through the flow depth, and are separated by a series of breaking-size-segregation waves. Diffusion can compete against this overturning effect. In particular, there is a region of parameter space where the diffusion and the secondary recirculation balance to create a stable wavy interface between large and small particles, which can suppress the development of surface compositional differences. In this regime, a depth-averaged theory for segregation is derived that captures the three-dimensional time-dependent development of the particle-size distribution from a uniformly inversely graded inflow into a series of transversely segregated stripes. The solution is in good quantitative agreement with the evolution of the surface particle-size distribution observed in experiments.

Key words: dry granular material, avalanches

© The Author(s), 2026. Published by Cambridge University Press. This is an Open Access article, distributed under the terms of the Creative Commons Attribution licence (https://creativecommons.org/licenses/by/4.0/), which permits unrestricted re-use, distribution and reproduction, provided the original article is properly cited.

https://doi.org/10.1017/jfm.2026.12176

1. Introduction

Longitudinal ridges and flow bands with different compositions have been observed in the deposits of large runout landslides on Earth (Shreve 1966; Post 1967; McSaveney 1978; Dufresne & Davies 2009; Magnarini *et al.* 2024), Mars (Magnarini *et al.* 2019, 2024) and the Moon (Magnarini *et al.* 2021*b*). Magnarini *et al.* (2019, 2021*b*, 2024) have argued that these features, which can extend for several kilometres in length, are likely due to the development of secondary recirculation within the granular flow. Pearse *et al.* (2026) recently developed a small-scale analogue experiment for such flows by using a size-bidisperse mixture of grains of the same intrinsic density, as shown in figure 1. The deposit is produced by releasing the mixture on a curved chute that gradually transitions from 46° at its steepest point to 17° at its shallowest point. This allows the grains to accelerate rapidly downslope, before decelerating and stopping. During flow, a diffuse fines-rich front forms ahead of alternating bands of large green and small white material, which are aligned with the flow direction. In the latter stages, the flow slows down and large grains rise to the surface and are preferentially transported to the flow front, which begins to finger before arresting (Pouliquen *et al.* 1997; Woodhouse *et al.* 2012; Baker *et al.* 2016). The deposit preserves the striped pattern and the large green front, and consists of evenly spaced stripes with approximate wavelength of $12 - 13$ mm between the centres of adjacent large–rich bands, which are themselves slightly raised above the finer grained troughs. The deposit was sectioned to show that the stripes extended all the way through the flow depth.

It is important to distinguish these bidisperse stripes from bidisperse fingered flows which may look superficially similar. As shown in movie 1, the stripes form within a rapid flow on a steep slope, when all the particles are in motion. In contrast, bidisperse fingered flows segregate large particles to the surface, preferentially transport them to the flow front and then deposit them into static levees on either side of the main channel (Pouliquen *et al.* 1997; Woodhouse *et al.* 2012; Baker *et al.* 2016; Rocha *et al.* 2019; Edwards *et al.* 2023). This also produces longitudinal large–rich bands, but the bands are formed at the flow front rather than internally, and these flows occur on shallow slopes where the grains naturally want to arrest. This regime only develops in the very final stages of the experiment illustrated in figure 1 and shown in movie 1.

Pearse *et al.* (2026) also developed a conceptual model to explain the formation of the stripes (figure 2*a*) with standard segregation theory (Gray 2018). It relies on the bulk flow developing a series of secondary vortices whose axes are aligned with the flow direction, as shown in figure 2(*b–d*). Each stripe, measured from centre to centre of adjacent large–rich bands, consists of two counter-rotating vortices. The magnitude of the cross-slope and slope-normal velocities are much lower than the downslope velocity. However, the secondary flow has a profound effect on the particle-size distribution, rotating what would otherwise be an inversely graded vertical layering, with large particles on top of fines (Gray 2018), into a series of alternating segregated bands that extend through the flow depth and are aligned with the flow direction. Pearse *et al.* (2026) performed experiments on a straight chute to generate a quasi-steady-state striped flow. In these experiments the spacing of the stripes was 10 mm and the flow depth was approximately 2.7 mm, giving a width to height aspect ratio of a single vortex cell of approximately 1.85. The origin of the secondary recirculation and what sets the wavelength remains an open question, but the premise in this paper is that the secondary recirculation is not driven by the segregation of the particles, but is a property of the bulk flow.

Forterre & Pouliquen (2001) developed experiments of a rapid, dilute, monodisperse granular flow down a rough inclined plane with solids volume fraction $\Phi \simeq 0.3$, which developed ridges parallel to the flow direction. Surface velocity measurements revealed

https://doi.org/10.1017/jfm.2026.12176



Figure 1. A photograph of the deposit formed by releasing a 30 : 70 mixture of large green (200−250 μm) and small white (60−150 μm) glass ballotini onto a curved chute that transitions from 46° at its steepest point to 17° at its shallowest point (Pearse *et al.* 2026). A hopper and two-gate system control the inflow, the first gate is set at 25 mm and the second gate is used to start the flow. The bed was originally roughened with a monolayer of spherical turquoise glass ballotini (750−1000 μm), which was stuck down with double-sided tape. Over time this has partially worn off to reveal the white tape. The deposit consists of alternating green and white stripes, which have high concentrations of large and small particles, respectively. The stripes are terminated by a large–rich front that has just started to finger before arresting. Movie 1, available in the online supplementary material at https://doi.org/10.1017/jfm.2026.12176, shows the time-dependent development of a similar deposit.

higher–slower regions and lower–faster regions, with surface particles migrating from the ridge crests to the troughs. Analogous to the Rayleigh–Bénard instability in fluids, Forterre & Pouliquen (2001) proposed a mechanism based on the strength of velocity fluctuations in the material. The flow's high speed and diluteness increased particle

https://doi.org/10.1017/jfm.2026.12176

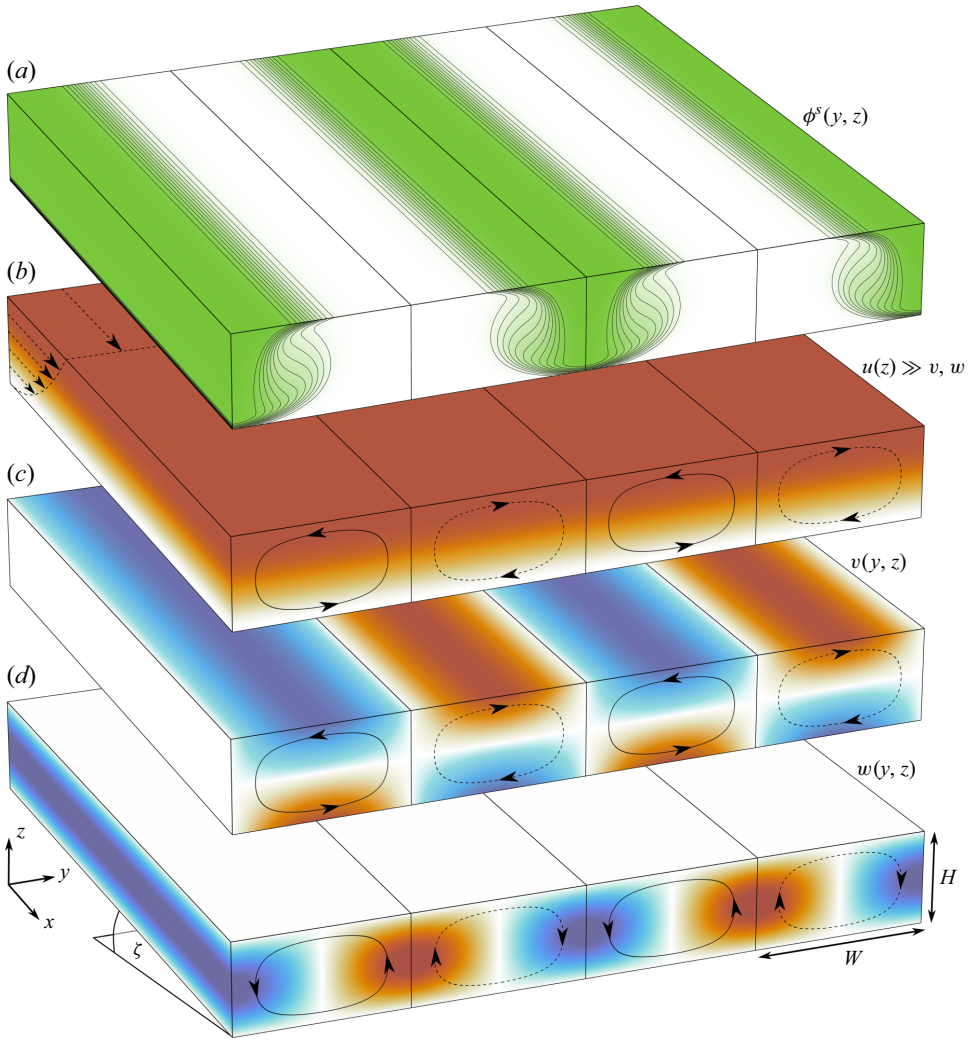


Figure 2. A simple conceptual model for the formation of two steady-uniform stripes measured from the centre to centre of adjacent large–rich bands. A coordinate system $Oxyz$ is defined on a plane that is inclined at an angle ζ to the horizontal. The x axis is oriented down the slope, the y axis lies across the slope and the z axis is parallel to the upward pointing normal. In panel (a) the small-particle concentration $\phi^s = \phi^s(y, z)$ is assumed to be independent of x. Regions of pure large (green) and pure small (white) particles form, which are separated by diffuse breaking-size-segregation waves (light green) (Thornton & Gray 2008; Gray & Ancey 2009; Edwards *et al.* 2023; Pearse *et al.* 2026). In panels (b–d) the downslope, cross-slope and normal velocity components of the prescribed velocity field $\boldsymbol{u} = (u, v, w)$ are shown. The downslope velocity $u(z) \gg v(y, z), w(y, z)$ and there are four counter-rotating secondary vortices oriented in the downslope direction x. A secondary vortex that is rotating anticlockwise/clockwise is drawn with solid/dashed arrowed line. The vortices are assumed to have a height H and width W.

collisions with the rough base, raising the granular temperature there and hence decreasing the density at the bottom of the flow to produce a granular Leidenfrost layer (Campbell 1989; Campbell *et al.* 1995; Eshuis *et al.* 2005; Taberlet *et al.* 2009). This led to an unstable density profile through the flow depth, which then broke down into a series of secondary vortices and longitudinal ridges. Forterre & Pouliquen (2002) used linear stability analysis to show that kinetic theory for granular gases (Jenkins & Savage 1983; Goldhirsch 2003)

https://doi.org/10.1017/jfm.2026.12176

was able to qualitatively capture the instability, but that it predicted the formation of vortices at much lower slope angles than was observed experimentally. In a similar regime, Brodu *et al.* (2013, 2015) performed discrete element method (DEM) simulations demonstrating the development of secondary flows in an inclined plane flow with rough sidewalls.

In contrast, Börzsönyi *et al.* (2009) showed the formation of longitudinal ridges in a dense flow with solids volume fraction $\Phi \in [0.36, 0.57]$. In this regime, the monodisperse granular flow developed higher–faster and lower–slower regions, both experimentally and in DEM simulations, with vortices rotating in the opposite direction to those in the dilute regime of Forterre & Pouliquen (2001), i.e. particles migrating from the troughs towards the ridges. The DEM simulations captured the dense regime for slope angles $\zeta \in [34^\circ, 39^\circ]$ revealing a low-density layer near the base of the flow which allows the dense, ridged layer to flow faster downstream. It therefore seems likely that the stripes observed by Pearse *et al.* (2026), and those presented in figure 1 and in § 6, lie in the dense regime of Börzsönyi *et al.* (2009).

The development of secondary vortices provides an important insight into the rheology of granular materials, which remains a highly active area of research (GDR-MiDi 2004; Jop *et al.* 2006; Kamrin & Koval 2012; Bouzid *et al.* 2013; Barker *et al.* 2015; Bouzid *et al.* 2015; Kamrin & Henann 2015; Barker & Gray 2017; Heyman *et al.* 2017; Schaeffer *et al.* 2019; Barker *et al.* 2021; Lloyd *et al.* 2025). In particular, McElwaine *et al.* (2012), Srivastava *et al.* (2021) and Kim & Kamrin (2023) have proposed an extension to the $\mu(I)$ rheology (in which the friction μ is a function of the inertial number $\boldsymbol{I}$, see Jop *et al.* 2006) that includes both first and second-normal-stress differences. In this rheology the second-order Cauchy stress tensor is

$$\boldsymbol{\sigma} = p\left(-\boldsymbol{I} + \frac{\mu_1}{\|\boldsymbol{D}\|}\left[\boldsymbol{D} - \frac{1}{3}\mathrm{tr}(\boldsymbol{D})\boldsymbol{I}\right] - \frac{\mu_2}{\|\boldsymbol{D}\|^2}\left[\boldsymbol{D}^2 - \frac{1}{3}\mathrm{tr}(\boldsymbol{D}^2)\boldsymbol{I}\right] - \frac{\mu_3}{\|\boldsymbol{D}\|^2}\mathring{\boldsymbol{D}}\right), \tag{1.1}$$

where $p = -\mathrm{tr}(\boldsymbol{\sigma})/3$ is the pressure, $\boldsymbol{I}$ is the unit tensor and $\boldsymbol{D} = (\nabla\boldsymbol{u} + \nabla\boldsymbol{u}^T)/2$ is the strain rate, which is defined in terms of the velocity gradient $\nabla\boldsymbol{u}$ and its transpose. The second invariant of the strain-rate tensor is defined as

$$\|\boldsymbol{D}\| = \sqrt{\frac{1}{2}\mathrm{tr}(\boldsymbol{D}^2)}, \tag{1.2}$$

and $\mathring{\boldsymbol{D}}$ is the Jaumann derivative

$$\mathring{\boldsymbol{D}} = \dot{\boldsymbol{D}} - \boldsymbol{W}\boldsymbol{D} + \boldsymbol{D}\boldsymbol{W}, \tag{1.3}$$

where $\dot{\boldsymbol{D}} = \partial\boldsymbol{D}/\partial t + (\boldsymbol{u}\cdot\nabla)\boldsymbol{D}$ is the material derivative, and the spin tensor $\boldsymbol{W} = (\nabla\boldsymbol{u} - \nabla\boldsymbol{u}^T)/2$. GDR-MiDi (2004) and Srivastava *et al.* (2021) used DEM simulations to show that, during flow, the coefficients μ_1, μ_2 and μ_3 are functions of the inertial number

$$I = \frac{2\,\|\boldsymbol{D}\|\,d}{\sqrt{p/\rho_*}}, \tag{1.4}$$

where d is the particle diameter and ρ_* is the intrinsic density of the grains. If μ_2 and μ_3 are zero, then this second-order rheology reduces to the classical $\mu(I)$ rheology of GDR-MiDi (2004) and Jop *et al.* (2006), which is not guaranteed to be mathematically well posed (Barker *et al.* 2015; Barker & Gray 2017; Heyman *et al.* 2017; Schaeffer *et al.* 2019). This is a concern if one wanted to use the model in time-dependent simulations, as there is no guarantee that they would stay in the well-posed region of parameter space, leading to catastrophic instabilities and grid-resolution-dependent results. On the other

https://doi.org/10.1017/jfm.2026.12176

hand, the model is interesting because the additional terms introduce first- and second-normal-stress differences, which can generate secondary vortices both in the presence and absence of gravity (Kim & Kamrin 2023; Levay *et al.* 2025).

The rheology (1.1) was used by Gadal *et al.* (2026) to derive an approximate steady-state solution for the incompressible flow in a transversely shallow parabolic channel. The second-normal-stress differences caused the flow to bow upwards in the centre of the channel, and generated two counter-rotating vortices with surface particles migrating towards the central ridge, as in Börzsönyi *et al.*'s (2009) experiments. Gadal *et al.*'s (2026) solution was in good quantitative agreement with experimental measurements and DEM simulations of the free-surface shape as well as DEM simulations of the downslope velocity, which was closely approximated by a series of adjacent Bagnold velocity profiles of variable depth. The secondary recirculation in the DEM simulations was also in good qualitative agreement with the asymptotic solution assuming shallow lateral curvature. This suggests that second-normal-stress differences play an important role in generating secondary vortices on an inclined plane, but this remains an open question, and dilatation near the base of the flow may play an important role in setting the direction of rotation, potentially enhancing or competing against the second-normal-stress difference mechanism. Indeed, Krishnaraj & Nott (2016) and Dsouza & Nott (2021) have also shown that even in slow flows dilation and gravity alone can drive secondary vortices.

D'Ortona & Thomas (2020, 2025) presented longitudinally striped experiments and DEM simulations formed by a size-bidisperse mixture with large particles that were more dense than small particles. Beginning from a flow with large–dense particles above small–light particles, the density differences triggered a Rayleigh–Taylor instability where large–dense particles on top are displaced by the small–light particles below. Simultaneously, particle-size segregation drives the large–dense particles back to the surface and small–light particles to the flow's base. This forms a series of re-circulating cells orientated with the flow direction, analogous to Rayleigh–Bénard convection cells. The process relies on a density difference between large and small particles, with D'Ortona & Thomas (2020) stating that no stripes were observed when the density of small and large particles was the same. However, the experiments in Pearse *et al.* (2026) demonstrate that a bidisperse flow with particles that differ in size, but not density, can generate stripes if the bulk flow already has an underlying secondary flow.

Given the uncertainties of the mechanisms driving the secondary recirculation, Pearse *et al.* (2026) prescribed it and focussed on how stable large– and small–rich flow bands are formed. In the absence of diffusion and assuming spatial uniformity in the downslope direction, Pearse *et al.* (2026) computed the time-dependent development of the particle-size distribution from an inversely graded initial state. They showed that the bulk flow rotates the sharp interface between large particles above, and small particles below, from the horizontal around to the vertical, so that large particles concentrate in the downwelling regions and small particles accumulate in the upwelling regions. As the interface approaches vertical, it forms a series of breaking-size-segregation waves (Thornton & Gray 2008; Gray & Ancey 2009; Gray & Kokelaar 2010*a*,*b*; Edwards *et al.* 2023). These waves grow until they reach the full cell height after which they oscillate backwards and forwards before reaching steady state.

The breaking-size-segregation waves allow the large particles that are rotated underneath fines to rise rapidly to the surface, while at the same time allowing small particles that are rotated above large grains to percolate downwards. In this way each secondary vortex of the bulk flow has two interpenetrating co-rotating sub-vortices of large and small particles that generate stable flow bands. Pearse *et al.* (2026) explicitly calculated

https://doi.org/10.1017/jfm.2026.12176

the structure of the breaking waves at steady state. The waves are similar to those found by Gray & Ancey (2009), but they occupy the full flow height, their axis of rotation is oriented in the downslope direction and they are stationary in the transverse plane. This contrasts with those found by Gray & Kokelaar (2010*a*,*b*) and Gray & Ancey (2009), which did not occupy the full flow depth, had their axis of rotation across the chute, moved steadily downslope and could merge with one another. Interestingly, in both situations it is the downslope shear that predominantly sets the magnitude of the segregation rate (Trewhela *et al.* 2021). As a result, in the transverse breaking waves studied by Pearse *et al.* (2026), the top of the wave moves downslope significantly faster than the base, generating complicated helical particle paths that were aligned with the downslope motion.

The aim of this paper is to extend the theory of Pearse *et al.* (2026) to include diffusive particle remixing. When there is sufficient diffusion, a longitudinally striped segregation pattern is not necessarily produced, because the lateral diffusion can oppose the overturning of the interface between large and small grains. As a result, flows with secondary vortices can also produce an inversely graded particle-size distribution. This poses the question of how many apparently mundane flows actually have secondary vortices present? The governing equations are presented in § 2 and specialised to the case of a single vortex cell that is spatially uniform in the downslope direction. In § 3 the resulting two-dimensional problem in the transverse plane is solved numerically over a wide range of parameter space. In particular, there is a region of parameter space where the interface between large and small particles is relatively sharp, even when diffusion is included. This motivates the derivation of a general depth-averaged segregation theory in § 4 that includes lateral diffusive terms (and allows spatial non-uniformity in the downslope direction). It is shown in § 5 that this theory can capture wavy steady states as well as the time-dependent motion of the sharp interface. In § 6 experiments are performed to investigate the development of the stripes along the length of the chute, and this is modelled with the depth-averaged theory in § 7.

2. Governing equations

2.1. *The segregation-advection-diffusion equation and boundary conditions*

Consider a bidisperse mixture of large and small particles flowing down a chute inclined at an angle ζ to the horizontal. Define a Cartesian coordinate system $Oxyz$ with the x-axis pointing downslope, the y-axis pointing in the cross-slope direction and the z-axis being the upward pointing normal. Unit vectors $\boldsymbol{i}$, $\boldsymbol{j}$ and $\boldsymbol{k}$ are defined in each of these directions. All the particles have the same intrinsic density ρ_* and the solids volume fraction Φ is assumed to be constant. The volume fraction of large and small particles per unit granular volume are defined as ϕ^l and ϕ^s, respectively. It follows that their sum is equal to unity

$$\phi^s + \phi^l = 1. \tag{2.1}$$

The particle concentrations ϕ^l and ϕ^s satisfy the segregation-advection-diffusion equations (Gray & Thornton 2005; Gray & Chugunov 2006; Gray & Ancey 2011; Gray 2018)

$$\frac{\partial \phi^l}{\partial t} + \boldsymbol{\nabla}\cdot\left(\phi^l \boldsymbol{u}\right) + \boldsymbol{\nabla}\cdot\left(f_{ls}\phi^l\phi^s\boldsymbol{e}\right) = \boldsymbol{\nabla}\cdot\left(D\boldsymbol{\nabla}\phi^l\right), \tag{2.2}$$

$$\frac{\partial \phi^s}{\partial t} + \boldsymbol{\nabla}\cdot\left(\phi^s \boldsymbol{u}\right) - \boldsymbol{\nabla}\cdot\left(f_{ls}\phi^s\phi^l\boldsymbol{e}\right) = \boldsymbol{\nabla}\cdot\left(D\boldsymbol{\nabla}\phi^s\right), \tag{2.3}$$

where $\boldsymbol{\nabla}$ is the gradient operator, $\cdot$ is the dot product, $\boldsymbol{u} = (u, v, w) = u\boldsymbol{i} + v\boldsymbol{j} + w\boldsymbol{k}$ is the bulk velocity field, f_{ls} is the segregation velocity magnitude, $\boldsymbol{e} = (e_x, e_y, e_z)$ is the unit

https://doi.org/10.1017/jfm.2026.12176

vector in the direction in which large particles segregate and D is the isotropic particle diffusion coefficient. The segregation direction will be discussed at greater length in § 4, but it is usually aligned in the opposite direction to the gravitational acceleration vector $\boldsymbol{g}$. When (2.2)–(2.3) are summed over all constituents, the summation condition (2.1) implies that the bulk velocity field $\boldsymbol{u}$ is incompressible

$$\boldsymbol{\nabla} \cdot \boldsymbol{u} = 0. \tag{2.4}$$

The system (2.2)–(2.3) can be reduced to a single equation for the small-particle concentration ϕ^s (say), by using the summation condition (2.1) to eliminate ϕ^l, to give

$$\frac{\partial \phi^s}{\partial t} + \boldsymbol{\nabla} \cdot (\phi^s \boldsymbol{u}) - \boldsymbol{\nabla} \cdot \left(f_{ls} \phi^s (1 - \phi^s) \boldsymbol{e} \right) = \boldsymbol{\nabla} \cdot (D \boldsymbol{\nabla} \phi^s). \tag{2.5}$$

The small-particle concentration therefore evolves in time due to advection by the bulk flow, downward segregation parallel to the direction $\boldsymbol{e}$ and isotropic diffusion. This is subject to a no-flux condition on the boundaries of the domain. Assuming that the bulk flow satisfies kinematic conditions on the free surface $z = s(x, y, t)$ and base $z = b(x, y, t)$ of the flow (see e.g. Savage & Hutter 1989; Gray *et al.* 2003), i.e. that

$$\frac{\partial s}{\partial t} + u \frac{\partial s}{\partial x} + v \frac{\partial s}{\partial y} - w = 0, \quad \text{on} \quad z = s(x, y, t), \tag{2.6}$$

$$\frac{\partial b}{\partial t} + u \frac{\partial b}{\partial x} + v \frac{\partial b}{\partial y} - w = 0, \quad \text{on} \quad z = b(x, y, t), \tag{2.7}$$

the no-flux condition for the small particles reduces to

$$f_{ls} \phi^s (1 - \phi^s) \boldsymbol{e} \cdot \boldsymbol{n} + D \boldsymbol{\nabla} \phi^s \cdot \boldsymbol{n} = 0, \quad \text{on} \quad z = s(x, y, t),\ b(x, y, t), \tag{2.8}$$

where $\boldsymbol{n} = (-\partial z/\partial x, -\partial z/\partial y, 1)$ is the normal to the free surface or base of the flow (see e.g. Gray & Chugunov 2006; Gray & Ancey 2011).

2.2. *Downslope uniformity*

The straight chute experiments of Pearse *et al.* (2026) suggest that the stripes are only weakly dependent on the downslope coordinate x. This motivates the simplification of the problem by assuming downslope uniformity of the particle concentration $\phi^s(y, z, t)$. Note that this assumption will be made for the theory developed here and the single-cell computations made in §§ 3 and 5, but is not made when developing the general depth-averaged theory in § 4 or when modelling the spatial development of the stripes along the chute in § 7. Throughout this paper the velocity is assumed to be independent of the downslope coordinate and independent of time, i.e. $\boldsymbol{u} = \boldsymbol{u}(y, z)$ as shown in figure 2. As a result the incompressibility condition (2.4) reduces to

$$\frac{\partial v}{\partial y} + \frac{\partial w}{\partial z} = 0, \tag{2.9}$$

and the segregation-advection-diffusion equation (2.5) becomes

$$\frac{\partial \phi^s}{\partial t} + \frac{\partial}{\partial y}(\phi^s v) + \frac{\partial}{\partial z}(\phi^s w) - \frac{\partial}{\partial z}\left(q \phi^s (1 - \phi^s) \right) = \frac{\partial}{\partial y}\left(D \frac{\partial \phi^s}{\partial y} \right) + \frac{\partial}{\partial z}\left(D \frac{\partial \phi^s}{\partial z} \right), \tag{2.10}$$

where the normal component of the small-particle segregation velocity is

$$q = f_{ls} \boldsymbol{e} \cdot \boldsymbol{k}. \tag{2.11}$$

https://doi.org/10.1017/jfm.2026.12176

In general, the segregation velocity q is linearly dependent upon the shear rate and the average particle diameter, and has further dependencies on the particle-size ratio, intrinsic particle density, pressure and the particle concentrations, while the diffusion coefficient D is linearly dependent on the shear rate and has a quadratic dependence on the average particle diameter (Savage & Lun 1988; Utter & Behringer 2004; Gray & Thornton 2005; Trewhela *et al.* 2021; Maguire *et al.* 2024). Since gradients of the secondary flow are much smaller than the downslope velocity gradient through the depth of the flow, the shear rate $\dot{\gamma} = 2\|\boldsymbol{D}\|$ is approximately equal to $|\partial u/\partial z|$. The downslope velocity profile therefore plays a dominant role in setting both the segregation rate and the diffusion, but does not appear explicitly in the equations.

2.3. *Assumed form of the secondary vortices*

The root cause of the secondary vortices is unclear and still a subject of active research. As discussed in the introduction, likely explanations are second-normal-stress differences (McElwaine *et al.* 2012; Srivastava *et al.* 2021; Kim & Kamrin 2023; Levay *et al.* 2025; Gadal *et al.* 2026) and/or the formation of a dilute Leidenfrost layer at the base of the avalanche which leads to instability and basal slip (Campbell 1989; Forterre & Pouliquen 2001; Eshuis *et al.* 2005; Börzsönyi *et al.* 2009; Wang *et al.* 2025). Following Pearse *et al.* (2026), the secondary vortices are parameterised in a simple way in order to solve for the associated segregation problem. The vortices are assumed to be rectangular in shape with incompressible bulk velocity field with transverse components

$$v = \Omega \sin\left(\frac{\pi y}{W}\right)(2z - H), \quad 0 \leqslant z \leqslant H, \quad mW \leqslant y \leqslant nW, \tag{2.12}$$

$$w = -\frac{\Omega \pi}{W} \cos\left(\frac{\pi y}{W}\right) z(z - H), \quad 0 \leqslant z \leqslant H, \quad mW \leqslant y \leqslant nW, \tag{2.13}$$

where Ω determines the rotation rate, H is the constant vortex height and W the constant vortex width, as shown in figure 2. A typical flow has $n-m$ counter-rotating vortices, where m and $n > m$ are integers. Each stripe measured from centre to centre of adjacent large–rich bands consists of two counter-rotating vortices. Note that this velocity field is constructed to be incompressible and satisfy the no normal flux condition $\boldsymbol{u} \cdot \boldsymbol{n} = 0$ on the cell boundaries. The cross-slope velocity (2.12) is non-zero at the base, i.e. basal slip is assumed. This is consistent with the experiments in § 6, which show that there is a significant amount of basal slip in the downslope direction. The slip could be facilitated by the formation of a low-density Leidenfrost layer at the base of the flow.

2.4. *Non-dimensionalisation*

In order to investigate the competing effects of segregation, secondary flow and diffusion, this paper assumes that the segregation velocity q and the diffusion coefficient D are constant. Introducing the non-dimensional variables, denoted by a tilde, via the scalings

$$(y, z) = H(\tilde{y}, \tilde{z}), \quad (v, w) = \Omega H(\tilde{v}, \tilde{w}), \quad t = (H/q)\tilde{t}, \tag{2.14}$$

where ΩH is a typical rotational velocity magnitude and H/q is a typical time scale for segregation to occur. These scalings imply the incompressibility condition (2.9) becomes

$$\frac{\partial \tilde{v}}{\partial \tilde{y}} + \frac{\partial \tilde{w}}{\partial \tilde{z}} = 0, \tag{2.15}$$

https://doi.org/10.1017/jfm.2026.12176

and the non-dimensional segregation-advection-diffusion equation (2.10) becomes

$$\frac{\partial \phi^s}{\partial \tilde{t}} + \frac{1}{\Lambda}\frac{\partial}{\partial \tilde{y}}(\phi^s \tilde{v}) + \frac{1}{\Lambda}\frac{\partial}{\partial \tilde{z}}(\phi^s \tilde{w}) - \frac{\partial}{\partial \tilde{z}}\big(\phi^s(1-\phi^s)\big) = \frac{1}{Pe}\left(\frac{\partial^2 \phi^s}{\partial \tilde{y}^2} + \frac{\partial^2 \phi^s}{\partial \tilde{z}^2}\right), \quad (2.16)$$

where the non-dimensional parameters

$$\Lambda = \frac{q}{\Omega H}, \quad \text{and} \quad Pe = \frac{qH}{D}, \quad (2.17a,b)$$

are the ratio of a typical segregation velocity to a typical vortex velocity and the ratio of a typical segregation velocity to a typical diffusive velocity, respectively. The scalings also imply that the no-flux boundary condition in (2.8) along the surface and base of the flow, when $\boldsymbol{n} = \pm\boldsymbol{k}$, becomes

$$\phi^s(1-\phi^s) + \frac{1}{Pe}\frac{\partial \phi^s}{\partial \tilde{z}} = 0, \quad \tilde{z} = 0,\, 1, \quad (2.18)$$

while on the sides of the flow (when $\boldsymbol{n} = \pm\boldsymbol{j}$) it reduces to the zero gradient condition

$$\frac{\partial \phi^s}{\partial \tilde{y}} = 0, \quad \tilde{y} = \tilde{W}m,\, \tilde{W}n, \quad (2.19)$$

provided that the segregation direction $\boldsymbol{e}$ does not have a component in the cross-slope direction, i.e. $\boldsymbol{e}\cdot\boldsymbol{j} = 0$. In addition an initial condition is required to solve for the small-particle concentration

$$\phi^s(\tilde{y}, \tilde{z}, 0) = \phi_0^s(\tilde{y}, \tilde{z}), \quad (\tilde{y}, \tilde{z}) \in [\tilde{W}m, \tilde{W}n] \times [0, 1]. \quad (2.20)$$

The non-dimensional scalings (2.14) imply that the velocity field (2.12)–(2.13) becomes

$$\tilde{v} = \sin\left(\frac{\pi \tilde{y}}{\tilde{W}}\right)(2\tilde{z} - 1), \quad 0 \leqslant \tilde{z} \leqslant 1, \quad \tilde{W}m \leqslant \tilde{y} \leqslant \tilde{W}n, \quad (2.21)$$

$$\tilde{w} = -\frac{\pi}{\tilde{W}}\cos\left(\frac{\pi \tilde{y}}{\tilde{W}}\right)\tilde{z}(\tilde{z} - 1), \quad 0 \leqslant \tilde{z} \leqslant 1, \quad \tilde{W}m \leqslant \tilde{y} \leqslant \tilde{W}n, \quad (2.22)$$

where $\tilde{W}$ is the non-dimensional width of the cell. In this paper it is assumed that $\tilde{W} = 1.85$, so that the velocity field is the same as that used by Pearse *et al.* (2026) in the absence of diffusion, and the vortex aspect ratio matches their straight chute experiments. Figure 7 of Pearse *et al.* (2026) shows a velocity vector plot, contour plots of the velocity components and the streamfunction for the velocity field above.

3. Two-dimensional numerical solutions in the cross-slope plane

3.1. *The numerical method*

Numerical solutions of the segregation-advection-diffusion equation (2.16) are obtained using the high-resolution central scheme of Kurganov & Tadmor (2000) with the Runge–Kutta–Chebyshev adaptive time-stepping method of Medovikov (1998). This time stepper is an efficient way of accounting for the stiffness of the system due to the presence of diffusion. The velocity field (2.21)–(2.22) is prescribed in a single vortical cell $(\tilde{y}, \tilde{z}) \in [0, 1.85] \times [0, 1]$. All simulations begin from an inversely graded initial state

$$\phi_0^s = \begin{cases} 0, & \tilde{z} > 0.7, \\ 1, & \tilde{z} \leqslant 0.7, \end{cases} \quad (3.1)$$

https://doi.org/10.1017/jfm.2026.12176

to reflect the 30 : 70 mix of large (green) and small (white) particles used in the experiments, and the no-flux boundary conditions (2.18) and (2.19) are applied at the edges of the domain.

3.2. *Time-dependent solutions with diffusion*

The evolution of a bidisperse mixture from an inversely graded initial distribution is shown in figure 3 for a single clockwise-rotating vortex cell. The flow has parameter values $(Pe, \Lambda) = (50, 1)$, which implies that the diffusion is relatively weak compared with the segregation, but that the vortical motion is comparable in magnitude. After $\tilde{t} = 0$, the sharp horizontal interface separating the large particles above, from the small particles below, is diffused and rotated by the velocity field (2.21)–(2.22). As in the case with no diffusion (see figure 8 of Pearse *et al.* 2026), the small particles concentrate in the upwelling part of the flow (on the left of the cell) and the large particles accumulate in the downwelling region (on the right of the cell), as shown in figure 3(*b*). The diffuse interface steepens and breaks at approximately $\tilde{t} = 1.4$ non-dimensional units, as shown in movie 2 in the online supplementary material, to form a diffuse breaking-size-segregation wave (figure 3*c*). This grows in height and width until it spans the full depth of the flow, and then oscillates backwards and forwards until it reaches steady state by approximately $\tilde{t} = 20$ non-dimensional time units. Although many features of the evolution towards steady state are similar to those in the absence of diffusion, the diffusion results in the interface between large and small particles being much less sharp, which may reflect real flows more accurately.

At steady state the diffuse breaking-size-segregation wave separates an almost pure upwelling region of small particles (on the left) from an almost pure downwelling region of large particles (on the right). The development of the breaking wave is crucial for the formation of longitudinal stripes that extend all the way through the flow depth, because it allows large particles that are advected under small particles to segregate back up towards the surface, and conversely allows small particles that are advected over large grains to percolate down towards the base. Pearse *et al.* (2026) showed that in the absence of diffusion, at steady state, the large- and small-particle paths form two interpenetrating co-rotating sub-vortices in the projected cross-slope plane, that allow stable stripes to be maintained. The full three-dimensional particle paths (taking into account the downslope motion) develop very complicated trajectories that depend strongly on the mixing ratio of the two species.

To aid understanding, a three-dimensional perspective view of the time-dependent computations in figure 3 is plotted in figure 4 for four counter-rotating vortex cells by using the symmetry of the solution. This shows how the evolving particle-size distribution in the $(\tilde{y}, \tilde{z})$-plane manifests itself at the free surface, which is the only thing that is visible in experiments. The initially inversely graded flow at $\tilde{t} = 0$ produces a green surface which persists at $\tilde{t} = 1$ even though the counter-rotating vortices have rotated the internal interface between large and small particles to form a diffuse wavy interface (figure 4*b*). It is only between $\tilde{t} = 2$ and 4 non-dimensional time units that small particles appear at the surface to form compositional stripes. The small white stripe is centred on the upwelling part of the flow, whereas the green large-particle bands are concentrated in the downwelling regions. The wave then oscillates backwards and forwards until a diffuse steady state is approached at $\tilde{t} = 20$, as can be seen in movie 3 in the online supplementary material. With these parameters the approximate 30 : 70 mixing ratio is reflected in the width of the steady-state large- and small-particle bands.

https://doi.org/10.1017/jfm.2026.12176

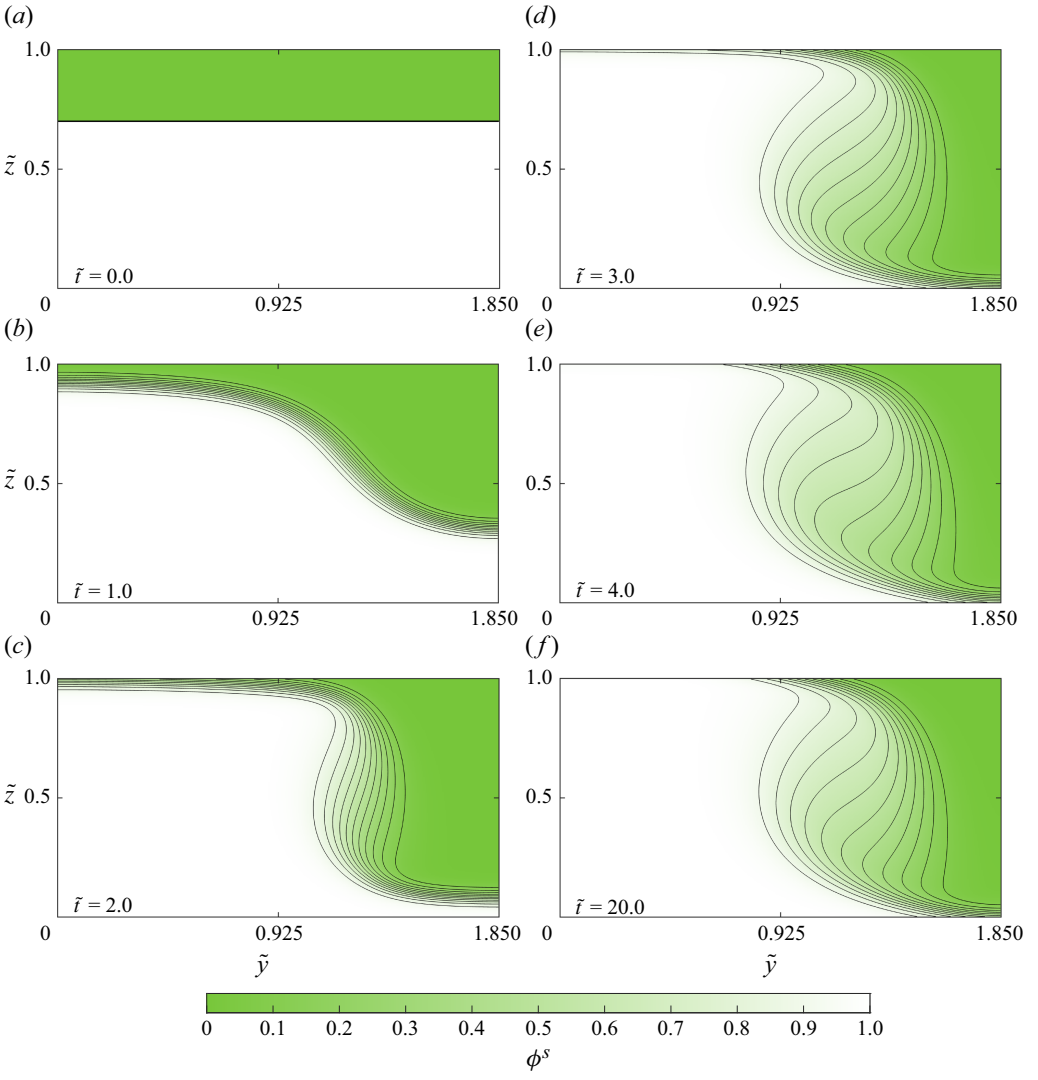


Figure 3. The evolution of the small-particle concentration ϕ^s at times (*a*) $\tilde{t} = 0$, (*b*) $\tilde{t} = 1$, (*c*) $\tilde{t} = 2$, (*d*) $\tilde{t} = 3$, (*e*) $\tilde{t} = 4$ and steady state (*f*) $\tilde{t} = 20$ for a 30 : 70 mix of large and small particles with parameter values $(Pe, \Lambda) = (50, 1)$. The solution is shown in a single clockwise-rotating secondary vortex cell with velocity field (2.21)–(2.22) applied. Movie 2 shows the complete time-dependent solution. The contour lines are shown in the range $\phi^s \in [0.1, 0.9]$ in 0.08 increments.

3.3. *The steady-state parameter space*

Steady-state solutions have been calculated for a wide range of values of the non-dimensional parameters Pe and Λ, and are shown in figure 5 for a 30 : 70 mix of large and small particles. The top row corresponds to the case investigated by Pearse *et al.* (2026), when there is no diffusion and $Pe = \infty$. Provided that there is some vortical motion (i.e. $\Lambda \neq \infty$) the flow has a pure band of large particles in the downwelling region and a pure band of small particles that is concentrated in the upwelling section, which are separated by a breaking-size-segregation wave that spans the full depth of the flow (Thornton & Gray 2008; Gray & Ancey 2009; Edwards *et al.* 2023; Pearse *et al.* 2026). As the strength of the

https://doi.org/10.1017/jfm.2026.12176

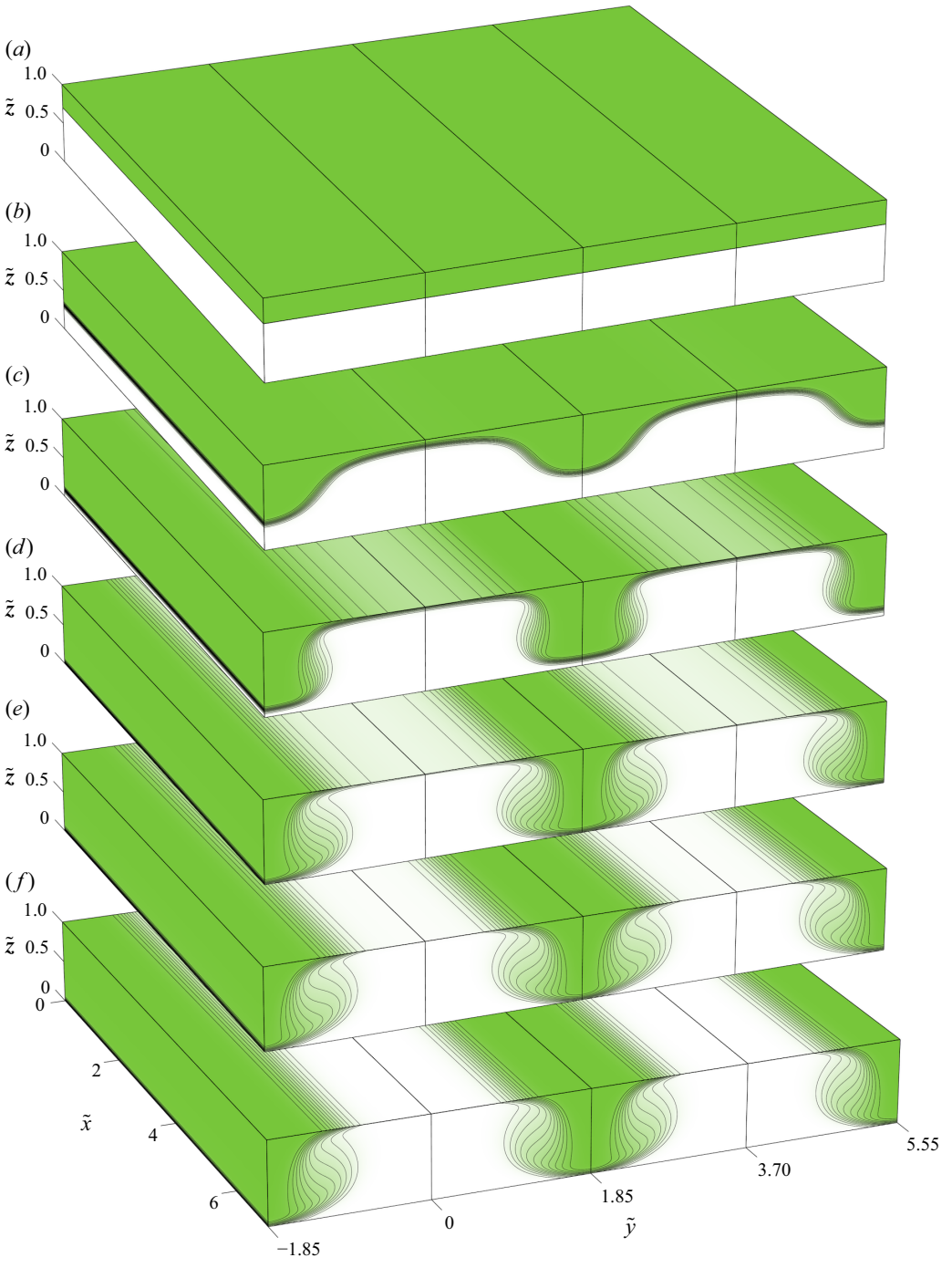


Figure 4. Perspective view of the time-dependent formation of two diffuse longitudinal stripes of large and small particles for $(Pe, \Lambda) = (50, 1)$ and a 30 : 70 mix. The solution spans four counter-rotating vortex cells. The small-particle concentration is shown at non-dimensional times (*a*) $\tilde{t} = 0$, (*b*) $\tilde{t} = 1$, (*c*) $\tilde{t} = 2$, (*d*) $\tilde{t} = 3$, (*e*) $\tilde{t} = 4$ and (*f*) $\tilde{t} = 20$ when the solution is close to steady state. The colour bar is the same as that in figure 3. Movie 3 shows the full time-dependent evolution. The contour lines are shown in the range $\phi^s \in [0.1, 0.9]$ in 0.08 increments.

https://doi.org/10.1017/jfm.2026.12176

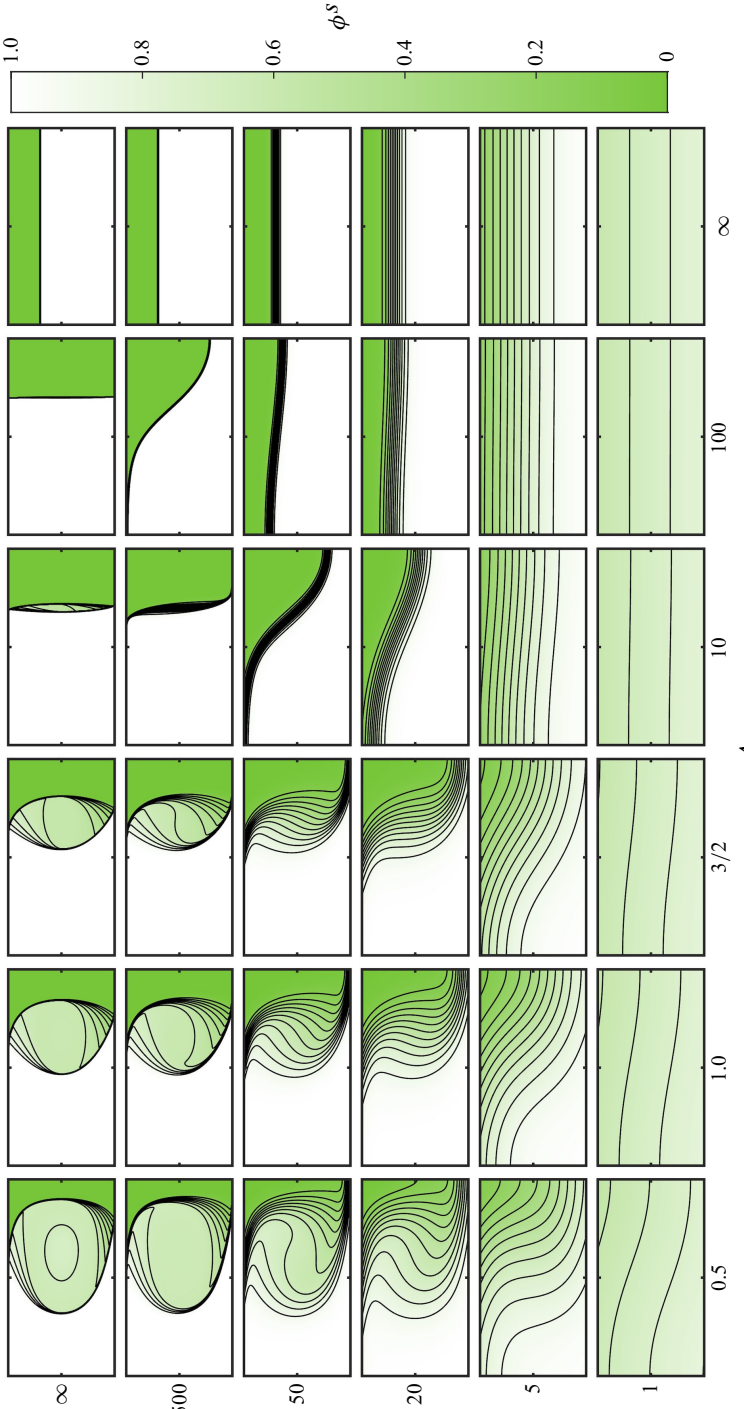


Figure 5. Steady-state solutions for the small-particle concentration ϕ^s for non-dimensional parameters $Pe = \infty$, 500, 50, 20, 5, 1 and $\Lambda = \infty$, 100, 10, 3/2, 1, 0.5 for a 30 : 70 mix of large and small particles. Increasing Pe corresponds to reducing the amount of diffusion compared with segregation, whereas increasing Λ corresponds to reducing the strength of the secondary flow relative to segregation. Each panel consists of a single clockwise-rotating vortex cell $[0, 1.85] \times [0, 1]$ with velocity field (2.21)–(2.22).

https://doi.org/10.1017/jfm.2026.12176

vortical motion decreases, which is equivalent to increasing Λ, the width of the breaking-size-segregation wave diminishes, so that as $\Lambda \to \infty$ it tends to a vertical shock separating large- and small-particle bands. The case when $\Lambda = \infty$ corresponds to no vortical motion, and is special. In this case, there is no rotational motion to steepen the interface between large and small particles, so it remains horizontal and separates the large particles above from the small particles below.

The right-hand column of figure 5 shows the effect of increasing the amount of diffusion in the absence of vortical motion, which is equivalent to decreasing Pe and holding $\Lambda = \infty$. These solutions are all inversely graded (i.e. large particles are concentrated near the surface and small particles are concentrated near the base), but the sharp shock that develops in the absence of diffusion is progressively diffused. These particle-size distributions are equivalent to the exact solution derived by Gray & Chugunov (2006) in their § 3.

The solutions in the second row of figure 5 have relatively weak diffusion. When the vortical motion is strong, i.e. Λ is low, the solutions look very similar to those in the absence of diffusion in the top row ($Pe = \infty$). However, as the vortical motion diminishes, the lateral diffusion can compete against the overturning effect of secondary flow, and a steady state develops with a relatively sharp 'S'-shaped interface between the large and small particles (see the case $Pe = 500$, $\Lambda = 100$). The ability of the lateral diffusion to balance the overturning effect of the secondary flow becomes progressively stronger as the strength of the diffusion is increased (i.e. Pe is decreased). Indeed for the case $Pe = 20$ and $\Lambda = 10$, the diffusion is strong enough to prevent small particles reaching the surface of the flow, so in an experiment one would not see the formation of stripes even though there was an underlying vortical flow. Note that, as the diffusion is increased, the 'S'-shaped interface between large and small particles becomes progressively more diffuse. Indeed, if the diffusion is too strong (e.g. for $Pe = 1$ in the bottom row) then it produces an almost uniform particle-size distribution throughout the cell.

4. General depth-averaged segregation theory with lateral diffusion

The steady-state solutions in § 3.3 suggest that there is a region of parameter space in which the interface between large and small particles remains fairly sharp, but that lateral diffusion can compete against the vortical motion to prevent it steepening to form a breaking-size-segregation wave. This suggests that it is possible to capture the approximate position of the interface with a depth-averaged segregation theory. Gray & Kokelaar (2010*a*,*b*) were the first to depth average the segregation equation (2.5). They showed that the resulting theory was able to exactly capture the sharp inversely graded interface between large and small particles in the absence of diffusion, as well as the approximate position of breaking-size-segregation waves, which were replaced with shocks (i.e. jumps in the interface height). The depth-averaged theory has the advantage that it takes one spatial dimension out of the problem and enables the direct coupling of particle segregation with depth-averaged theories for the bulk flow. Woodhouse *et al.* (2012) and Baker *et al.* (2016) used this approach to model the formation of segregation-induced flow fingers when large particles are more frictional than the fines.

The general depth-averaged theory is developed from the full segregation equation (2.5), and assumes that the small-particle concentration ϕ^s is no longer spatially uniform in the downslope direction. Integrating (2.5) through the avalanche depth, between $z = b(x, y, t)$ and $z = s(x, y, t)$, and exchanging the order of integration and differentiation by using Leibniz's rule (Abramowitz & Stegun 1970), implies

https://doi.org/10.1017/jfm.2026.12176

$$\frac{\partial}{\partial t}(h\overline{\phi^s}) + \frac{\partial}{\partial x}(h\overline{\phi^s u}) + \frac{\partial}{\partial y}(h\overline{\phi^s v}) - \left[\phi^s\left(\frac{\partial z}{\partial t} + u\frac{\partial z}{\partial x} + v\frac{\partial z}{\partial y} - w\right)\right]_b^s$$
$$- \frac{\partial}{\partial x}\left(\int_b^s f_{ls}\phi^s(1-\phi^s)e_x\,\mathrm{d}z\right) - \frac{\partial}{\partial y}\left(\int_b^s f_{ls}\phi^s(1-\phi^s)e_y\,\mathrm{d}z\right)$$
$$= \frac{\partial}{\partial x}\left(\int_b^s D\frac{\partial\phi^s}{\partial x}\,\mathrm{d}z\right) + \frac{\partial}{\partial y}\left(\int_b^s D\frac{\partial\phi^s}{\partial y}\,\mathrm{d}z\right) + \left[f_{ls}\phi^s(1-\phi^s)\boldsymbol{e}\cdot\boldsymbol{n} + D\nabla\phi^s\cdot\boldsymbol{n}\right]_b^s, \tag{4.1}$$

where the flow height

$$h = s(x, y, t) - b(x, y, t), \tag{4.2}$$

and the depth-averaged small-particle concentration and the depth-averaged small-particle fluxes in the down and cross-slope directions are

$$\overline{\phi^s} = \frac{1}{h}\int_b^s \phi^s\,\mathrm{d}z, \quad \overline{\phi^s u} = \frac{1}{h}\int_b^s \phi^s u\,\mathrm{d}z, \quad \overline{\phi^s v} = \frac{1}{h}\int_b^s \phi^s v\,\mathrm{d}z, \tag{4.3a,b,c}$$

respectively. The square bracketed terms in (4.1) are zero due to the kinematic conditions, (2.6) and (2.7), as well as the no small-particle flux condition (2.8). For simplicity, the segregation direction $\boldsymbol{e}$ is assumed to align with the slope normal $\boldsymbol{k}$, which eliminates the terms on the middle line of equation (4.1). This is equivalent to assuming that the segregation direction aligns with the pressure gradient through a steady uniform-depth flow. Alternatively, these terms can be eliminated by assuming that the segregation aligns with gravity, but the components in the down- and cross-slope directions are small enough to be neglected (Gray & Kokelaar 2010*a*,*b*; Barker *et al.* 2021; Maguire *et al.* 2024). With these assumptions (4.1) reduces to

$$\frac{\partial}{\partial t}(h\overline{\phi^s}) + \frac{\partial}{\partial x}(h\overline{\phi^s u}) + \frac{\partial}{\partial y}(h\overline{\phi^s v}) = \frac{\partial}{\partial x}\left(\int_b^s D\frac{\partial\phi^s}{\partial x}\,\mathrm{d}z\right) + \frac{\partial}{\partial y}\left(\int_b^s D\frac{\partial\phi^s}{\partial y}\,\mathrm{d}z\right). \tag{4.4}$$

The terms on the left-hand side are the same as those derived by Gray & Kokelaar (2010*a*,*b*) and Woodhouse *et al.* (2012), but the terms on the right, which capture the depth-averaged effect of lateral diffusion, are new. In order to apply the theory specific forms need to be derived for the integrals in (4.3) and those on the right-hand side of (4.4).

5. One-dimensional depth-averaged theory for transverse segregation

5.1. *Basic assumptions*

The theory is now reduced to the case in which there is no basal topography, $b = 0$, and the free surface lies at a constant height $h = s = H$. Furthermore, the stripes and the velocity field are assumed to be uniform in the downslope direction, so that the x-derivatives are zero, and the diffusion coefficient D is assumed to be constant. In this case (4.4) reduces to

$$\frac{\partial}{\partial t}(H\overline{\phi^s}) + \frac{\partial}{\partial y}(H\overline{\phi^s v}) = \frac{\partial}{\partial y}\left(D\frac{\partial}{\partial y}(H\overline{\phi^s})\right). \tag{5.1}$$

Following Gray & Kokelaar (2010*a*,*b*), and based on the simulations in § 3 that show there is a region of parameter space where the interface between large and small particles

https://doi.org/10.1017/jfm.2026.12176

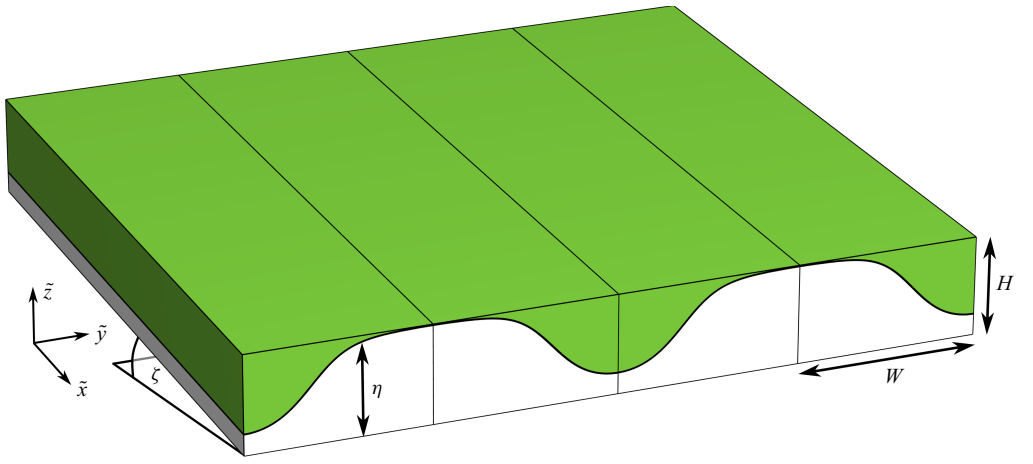


Figure 6. Schematic diagram of a bidisperse granular flow with a sharp interface η separating the large and small particles from one another. The flow spans four counter-rotating vortex cells with the steady-state solution to the depth-averaged theory shown for parameter values $(Pe, \Lambda) = (500, 100)$. The flow is inclined at angle ζ to the horizontal.

is relatively sharp, the small-particle concentration may reasonably be approximated by

$$\phi^s = \begin{cases} 0, & \eta < z \leqslant H, \\ 1, & 0 \leqslant z \leqslant \eta, \end{cases} \tag{5.2}$$

where η is the inversely graded interface height between large and small particles, as sketched in figure 6. It follows that the depth-averaged concentration, defined in (4.3*a*), satisfies

$$H\overline{\phi^s} = \eta. \tag{5.3}$$

An approximation for $\overline{\phi^s v}$ can be found by substituting the small-particle concentration (5.2) and the cross-slope velocity (2.12) into the integral (4.3*c*) to give

$$H\overline{\phi^s v} = \Omega \sin\left(\frac{\pi y}{W}\right)(\eta^2 - H\eta). \tag{5.4}$$

Substituting the integrals (5.3) and (5.4) into (5.1) implies that the depth-averaged segregation equation for the interface height η is

$$\frac{\partial \eta}{\partial t} + \frac{\partial}{\partial y}\left(\Omega \sin\left(\frac{\pi y}{W}\right)(\eta^2 - H\eta)\right) = \frac{\partial}{\partial y}\left(D\frac{\partial \eta}{\partial y}\right). \tag{5.5}$$

The quadratic structure of the small-particle flux on the left-hand side, implies that this equation will seek to segregate the large and small particles in the y direction, but as opposed to earlier theories, there is a diffusive flux on the right-hand side that can prevent the interface from steepening up to the vertical (Gray & Kokelaar 2010*a*,*b*; Woodhouse *et al.* 2012; Baker *et al.* 2016).

5.2. *Non-dimensionalisation*

The depth-averaged model is non-dimensionalised using the scalings in (2.14) and

$$\eta = H\tilde{\eta}, \tag{5.6}$$

https://doi.org/10.1017/jfm.2026.12176

to give the non-dimensional depth-averaged segregation-diffusion equation

$$\frac{\partial \tilde{\eta}}{\partial \tilde{t}} + \frac{1}{\Lambda}\frac{\partial}{\partial \tilde{y}}\left(\sin\left(\frac{\pi \tilde{y}}{\tilde{W}}\right)(\tilde{\eta}^2 - \tilde{\eta})\right) = \frac{1}{Pe}\left(\frac{\partial^2 \tilde{\eta}}{\partial \tilde{y}^2}\right), \tag{5.7}$$

where Pe and Λ are defined in (2.17). This is the depth-averaged equivalent to the two-dimensional segregation-diffusion equation (2.16). It is subject to a zero gradient boundary condition at the cell interfaces

$$\frac{\partial \tilde{\eta}}{\partial \tilde{y}} = 0 \quad \text{at} \qquad \tilde{y} = 0,\, \tilde{W}, \tag{5.8}$$

and an initial condition for the interface position

$$\tilde{\eta}(\tilde{y},\, 0) = \tilde{\eta}_0(\tilde{y}), \quad \tilde{y} \in [0,\, \tilde{W}], \tag{5.9}$$

where $\tilde{\eta}_0$ is the initial interface height.

5.3. *Depth-averaged numerical solutions for the interface*

Depth-averaged numerical solutions for the interface are obtained using the same shock-capturing numerical method as § 3.1. Computations are performed for a single depth-averaged vortex cell $\tilde{y} \in [0,\, 1.85]$ with no-flux boundary conditions (5.8) applied at each end of the domain. For consistency, a 30 : 70 mix of large and small particles is used, that is assumed to have a uniform inversely graded distribution across the cell, i.e. the initial interface height

$$\tilde{\eta}_0 = 0.7, \quad \tilde{y} \in [0,\, 1.85]. \tag{5.10}$$

To investigate the depth-averaged model's ability to capture the sharp interface, the case when $(Pe,\, \Lambda) = (500,\, 100)$ is studied. Figure 7(*a–e*) shows the time-dependent evolution of the one-dimensional interface $\tilde{\eta}$ and the corresponding two-dimensional particle-size distribution calculated using the full two-dimensional model developed in § 3. Initially the interface between the large and small particles starts off horizontal, but it is gradually rotated by the secondary flow, so that large particles concentrate in the downwelling region on the right, and the small particles concentrate in the upwelling region on the left. The diffusion is weak compared with the segregation, so the interface in the two-dimensional simulation stays sharp, and is well approximated by the one-dimensional depth-averaged theory throughout the entire time-dependent development, which can be seen in movie 4. The lateral diffusion is, however, strong enough to prevent the interface steepening up to the vertical and forming a breaking-size-segregation wave. The depth-averaged theory, and the full two-dimensional theory, therefore slowly approach a steady state with an 'S'-shaped interface by $\tilde{t} = 500$ non-dimensional time units. The exact steady-state solution is calculated in § 5.4 and is in excellent agreement with both computations. At steady state there is a thin layer of large particles on the surface of the upwelling region, but they are mainly concentrated in the downwelling region. In contrast, at steady state there is still quite a thick layer of small particles at the base of the downwelling region.

Figure 7(*f–j*) shows a similar simulation for $(Pe,\, \Lambda) = (500,\, 3/2)$. The relative strength of the diffusion to segregation is the same, but the secondary recirculation is significantly stronger. In this case the initial motion of the interface is also excellently captured by the depth-averaged theory, but at approximately $\tilde{t} = 2$ the interface breaks to form a diffuse breaking-size-segregation wave (Thornton & Gray 2008; Gray & Ancey 2009; Gray & Kokelaar 2010*a*,*b*; Pearse *et al.* 2026), which is not captured in the one-dimensional model. The two-dimensional simulations show that the breaking wave grows until it reaches the full height of the cell, and then it slowly oscillates backwards and forwards

https://doi.org/10.1017/jfm.2026.12176

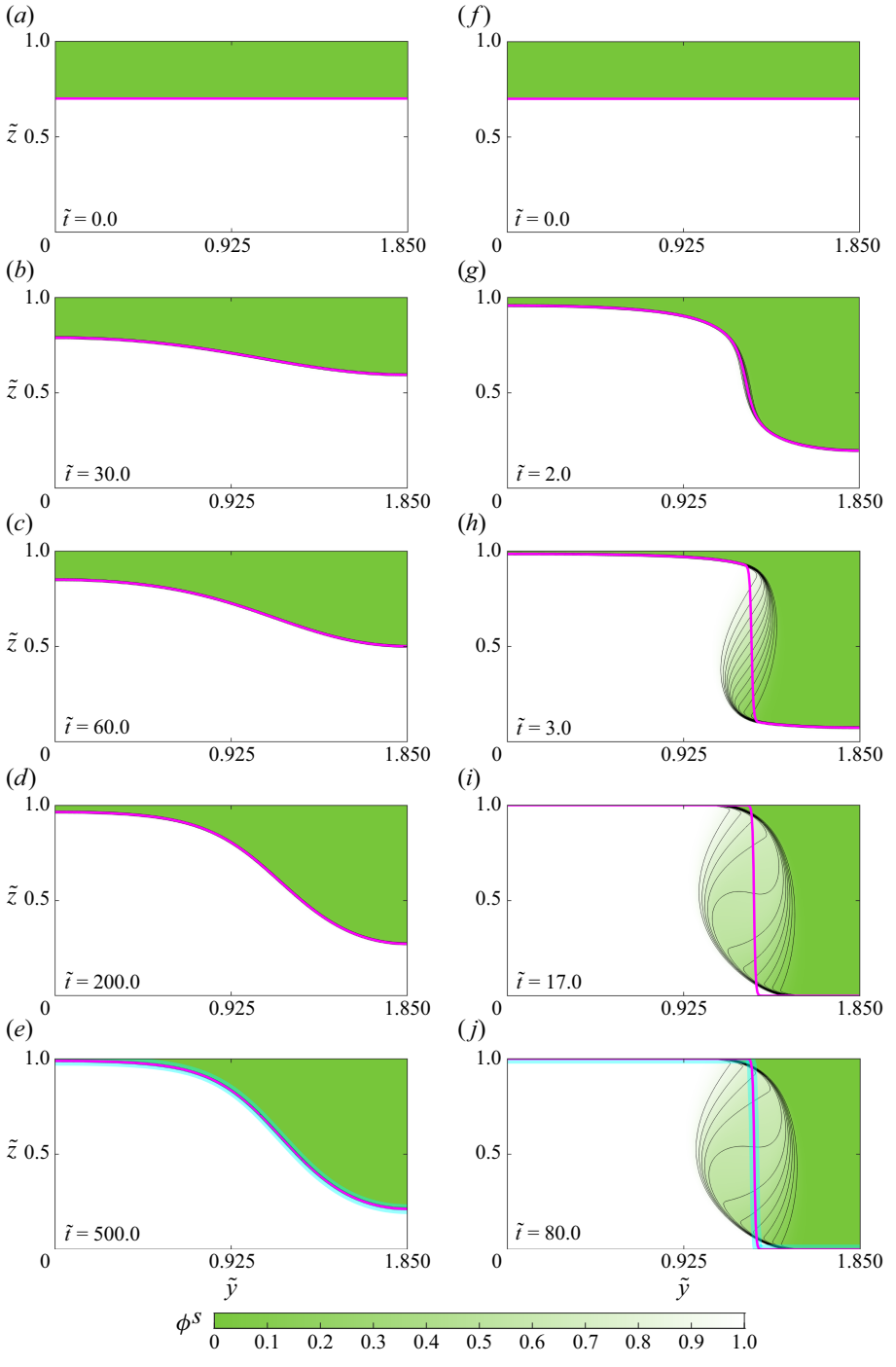


Figure 7. Comparison of the one-dimensional interface height $\tilde{\eta}$ (magenta line) between large and small particles, and the full two-dimensional solution for the concentration ϕ^s in a single clockwise-rotating vortex cell, with the velocity field (2.21)–(2.22), and for a 30 : 70 mix. Panels (*a*)–(*e*) show the time-dependent evolution for $(Pe,\ \Lambda) = (500,\ 100)$, while panels (*f*)–(*j*) show the solution for $(Pe,\ \Lambda) = (500,\ 3/2)$. The steady-state exact solutions are also shown for (*e*) $\Xi = 2.94$ and (*j*) $\Xi = 196.29$ (thicker semi-transparent light blue line). Movies 4 and 5 show the complete time-dependent evolution. The contour lines are shown in the range $\phi^s \in [0.1,\ 0.9]$ in 0.08 increments.

https://doi.org/10.1017/jfm.2026.12176

before settling down to a steady state. Despite the formation of the breaking wave, the one-dimensional model accurately captures the position of the sharp inversely graded interface, away from the breaking wave, during the subsequent evolution. In this case, the large-particle layer at the surface of the flow is so thin in the upwelling region that it can barely be seen, and the large particles concentrate throughout the entire depth of the downwelling region. Although the depth-averaged theory cannot capture the structure of the breaking-size-segregation wave, it does accurately capture its approximate position. The full time-dependent evolution of both models are shown in movies 4 and 5.

5.4. *Steady-state solution for the 'S'-shaped interface*

At steady state, an exact one-dimensional depth-averaged solution can be derived for the interface $\tilde{\eta}$. In this case the depth-averaged segregation-diffusion equation becomes

$$\frac{1}{\Lambda}\frac{d}{\mathrm{d}\tilde{y}}\left(\sin\left(\frac{\pi\tilde{y}}{\tilde{W}}\right)(\tilde{\eta}^2-\tilde{\eta})\right)=\frac{1}{Pe}\left(\frac{d^2\tilde{\eta}}{\mathrm{d}\tilde{y}^2}\right), \tag{5.11}$$

and since Pe and Λ are constant, this can be integrated once with respect to $\tilde{y}$. Applying the boundary condition (5.8) at $\tilde{y}=0$ (say), yields the ordinary differential equation (ODE)

$$\frac{\mathrm{d}\tilde{\eta}}{\mathrm{d}\tilde{y}}=\frac{Pe}{\Lambda}\sin\left(\frac{\pi\tilde{y}}{\tilde{W}}\right)(\tilde{\eta}^2-\tilde{\eta}). \tag{5.12}$$

This is separable, and can be integrated to give the exact solution

$$\tilde{\eta}=\frac{1}{1+A\exp\left(-\Xi\cos\left(\dfrac{\pi\tilde{y}}{\tilde{W}}\right)\right)}, \tag{5.13}$$

where A is a constant of integration and the non-dimensional parameter

$$\Xi=\frac{Pe\tilde{W}}{\pi\Lambda}=\frac{HW\Omega}{\pi D} \tag{5.14}$$

sets the non-dimensional length scale of the S-shaped interface. It can be thought of as a ratio of a typical circulation velocity to the velocity induced by lateral diffusion, and is independent of the segregation rate q. Moreover, since Pe and Λ appear as a ratio, it follows that the steady-state theory has the same interface shape for the same value of Pe/Λ. For instance, the shape of the interface for $(Pe,\ \Lambda)=(500,\ 100)$ is exactly the same as for $(Pe,\ \Lambda)=(50,\ 10)$, as illustrated in figure 5, although in the latter case the particle-size distribution is more diffuse in the full model, due to the lower value of Pe. Note that low values of Ξ generate smooth wavy inversely graded interfaces that do not approach the free surface, whereas high values of Ξ correspond to solutions in which stripes will be visible at the free surface, as shown in figure 7(*e*, *j*), respectively.

The constant of integration A in (5.13) is determined iteratively, by enforcing that the total volume of small grains in the secondary vortex is conserved, i.e. that

$$\int_0^{\tilde{W}}\tilde{\eta}\,\mathrm{d}\tilde{y}=\tilde{W}\tilde{\eta}_0. \tag{5.15}$$

As already shown in § 5.3, the exact solution (5.13) accurately predicts the final steady-state interface position provided that the secondary recirculation and the diffusion are not too strong compared with the segregation rate (e.g. for $(Pe,\ \Lambda)=(500,\ 100)$ in figure 7*e*). Importantly, this shows that, even if secondary vortices develop in the flow, it does not necessarily mean that compositional stripes will be seen at the surface of the

https://doi.org/10.1017/jfm.2026.12176

experiment, because the overturning effect can be balanced by lateral diffusion. Many apparently mundane flows may therefore have more complex underlying motion that is hard to spot. Note also that, if the recirculation becomes too strong, then the sharp interface between large and small particles becomes unstable and forms a breaking-size-segregation wave, which is not captured by the depth-averaged theory (e.g. for $(Pe, \Lambda) = (500, 3/2)$ in figure 7*f–j*). Nevertheless, the exact steady-state solution (5.13) is still able to approximate the position of the breaking wave, and accurately captures the interface outside of its immediate vicinity. The depth-averaged theory may therefore still provide useful predictions even outside the region of parameter space for which it was originally derived.

5.5. *Solving for the time-dependent evolution in the absence of diffusion*

It is also possible to derive an exact solution for the evolving interface in the absence of diffusion. In this case the depth-averaged segregation equation (5.7) reduces to

$$\frac{\partial \tilde{\eta}}{\partial \tilde{t}} + \frac{1}{\Lambda}\frac{\partial}{\partial \tilde{y}}\left(\sin\left(\frac{\pi \tilde{y}}{\tilde{W}}\right)(\tilde{\eta}^2 - \tilde{\eta})\right) = 0. \tag{5.16}$$

In quasi-linear form this is equivalent to

$$\frac{\partial \tilde{\eta}}{\partial \tilde{t}} + \frac{1}{\Lambda}\sin\left(\frac{\pi \tilde{y}}{\tilde{W}}\right)(2\tilde{\eta} - 1)\frac{\partial \tilde{\eta}}{\partial \tilde{y}} = -\frac{1}{\Lambda}\frac{\pi}{\tilde{W}}\cos\left(\frac{\pi \tilde{y}}{\tilde{W}}\right)(\tilde{\eta}^2 - \tilde{\eta}), \tag{5.17}$$

which can be solved by the method of characteristics. Introducing the variable λ to parameterise the characteristic curve $(\tilde{t}(\lambda), \tilde{y}(\lambda))$, then the rate of change of the interface along the characteristic curve is

$$\frac{\mathrm{d}\tilde{\eta}}{\mathrm{d}\lambda} = \frac{\partial \tilde{\eta}}{\partial \tilde{t}}\frac{\mathrm{d}\tilde{t}}{\mathrm{d}\lambda} + \frac{\partial \tilde{\eta}}{\partial \tilde{y}}\frac{\mathrm{d}\tilde{y}}{\mathrm{d}\lambda}. \tag{5.18}$$

Comparing (5.17) with (5.18) implies the characteristic equations are

$$\frac{\mathrm{d}\tilde{t}}{\mathrm{d}\lambda} = 1, \tag{5.19}$$

$$\frac{\mathrm{d}\tilde{y}}{\mathrm{d}\lambda} = \frac{1}{\Lambda}\sin\left(\frac{\pi \tilde{y}}{\tilde{W}}\right)(2\tilde{\eta} - 1), \tag{5.20}$$

$$\frac{\mathrm{d}\tilde{\eta}}{\mathrm{d}\lambda} = -\frac{1}{\Lambda}\frac{\pi}{\tilde{W}}\cos\left(\frac{\pi \tilde{y}}{\tilde{W}}\right)(\tilde{\eta}^2 - \tilde{\eta}). \tag{5.21}$$

Since λ does not appear on the right-hand side of this system, the chain rule and (5.19) can be used to eliminate it from (5.20) and (5.21), to generate the reduced system of two ODEs

$$\frac{\mathrm{d}\tilde{y}}{\mathrm{d}\tilde{t}} = \frac{1}{\Lambda}\sin\left(\frac{\pi \tilde{y}}{\tilde{W}}\right)(2\tilde{\eta} - 1), \tag{5.22}$$

$$\frac{\mathrm{d}\tilde{\eta}}{\mathrm{d}\tilde{t}} = -\frac{1}{\Lambda}\frac{\pi}{\tilde{W}}\cos\left(\frac{\pi \tilde{y}}{\tilde{W}}\right)(\tilde{\eta}^2 - \tilde{\eta}), \tag{5.23}$$

which are subject to the initial conditions

$$\tilde{y} = \tilde{y}_0, \qquad \text{and} \qquad \tilde{\eta} = \tilde{\eta}_0, \qquad \text{at} \qquad \tilde{t} = 0. \tag{5.24}$$

https://doi.org/10.1017/jfm.2026.12176

The chain rule can also be used to eliminate $\tilde{t}$, and the resulting separable ODE can be integrated to show that

$$\sin\left(\frac{\pi\tilde{y}}{\tilde{W}}\right)(\tilde{\eta}^2-\tilde{\eta})=\psi_0, \tag{5.25}$$

where ψ_0 is a constant of integration. Since the streamfunction for the non-dimensional velocity field (2.21)–(2.22), evaluated at the interface $\tilde{\eta}$, is

$$\psi=\sin\left(\frac{\pi\tilde{y}}{\tilde{W}}\right)(\tilde{\eta}^2-\tilde{\eta}), \tag{5.26}$$

equation (5.25) is equivalent to

$$\psi=\psi_0. \tag{5.27}$$

The characteristic curves therefore correspond to the closed streamlines of the bulk flow field. To solve for the position of the interface along the streamline at any given time, it is actually easier to solve the whole system (5.22)–(5.23) numerically. The initial interface position (5.24) is therefore parameterised by a series of points, whose subsequent motion is calculated by solving (5.22)–(5.23). Figure 8 and movie 6 show a comparison of the time-dependent evolution of the interface, solved by the method of characteristics, and the full two-dimensional solution for ϕ^s for parameters $(Pe,\,\Lambda)=(\infty,\,100)$. The depth-averaged solution accurately picks off the steepening of the sharp interface up to approximately $\tilde{t}=140$ non-dimensional time units, when the interface in the non-depth-averaged simulation breaks to form a very thin breaking-size-segregation wave. At subsequent times the interface position can still be calculated by the method of characteristics, but the solution is multi-valued. A shock, or discontinuity in the interface height, then develops, which connects two smooth single-valued branches of the solution.

The growth and dynamics of the shock are controlled by a jump condition (Whitham 1974; Chadwick 1976; Gray & Kokelaar 2010*a*,*b*). The jump condition is derived from the conservative form of the depth-averaged segregation equation (5.16), and in this case is

$$-v_n\left[\!\left[\tilde{\eta}\right]\!\right]+\left[\!\left[\frac{1}{\Lambda}\sin\left(\frac{\pi\tilde{y}}{\tilde{W}}\right)(\tilde{\eta}^2-\tilde{\eta})\right]\!\right]=0, \tag{5.28}$$

where v_n is the shock propagation speed and the jump bracket $[\![f]\!]=f_+-f_-$ is the difference of the enclosed quantity on the forward and rearward sides of the shock. This implies the shock speed is

$$v_n=\frac{1}{\Lambda}\sin\frac{\pi\tilde{y}}{\tilde{W}}(\tilde{\eta}_+ +\tilde{\eta}_- -1)=\frac{d\tilde{y}}{d\tilde{t}}, \tag{5.29}$$

which requires a knowledge of $\tilde{\eta}_+$ and $\tilde{\eta}_-$ across the shock, making it difficult to use directly. Instead, a shock fitting procedure is used to determine the shock position. This ensures that the lobes formed by the multi-valued characteristic solution, and which are cutoff by the shock, are of equal area (Whitham 1974). The shock forms at the point where the interface becomes vertical, and grows in height as the secondary vortex continues to steepen the interface between large and small particles. By $\tilde{t}=510$ non-dimensional time units, the shock reaches the full height of the cell and a steady state develops. Throughout the entire time-dependent evolution, the depth-averaged theory closely matches the position of the interface calculated with the full two-dimensional segregation theory.

https://doi.org/10.1017/jfm.2026.12176

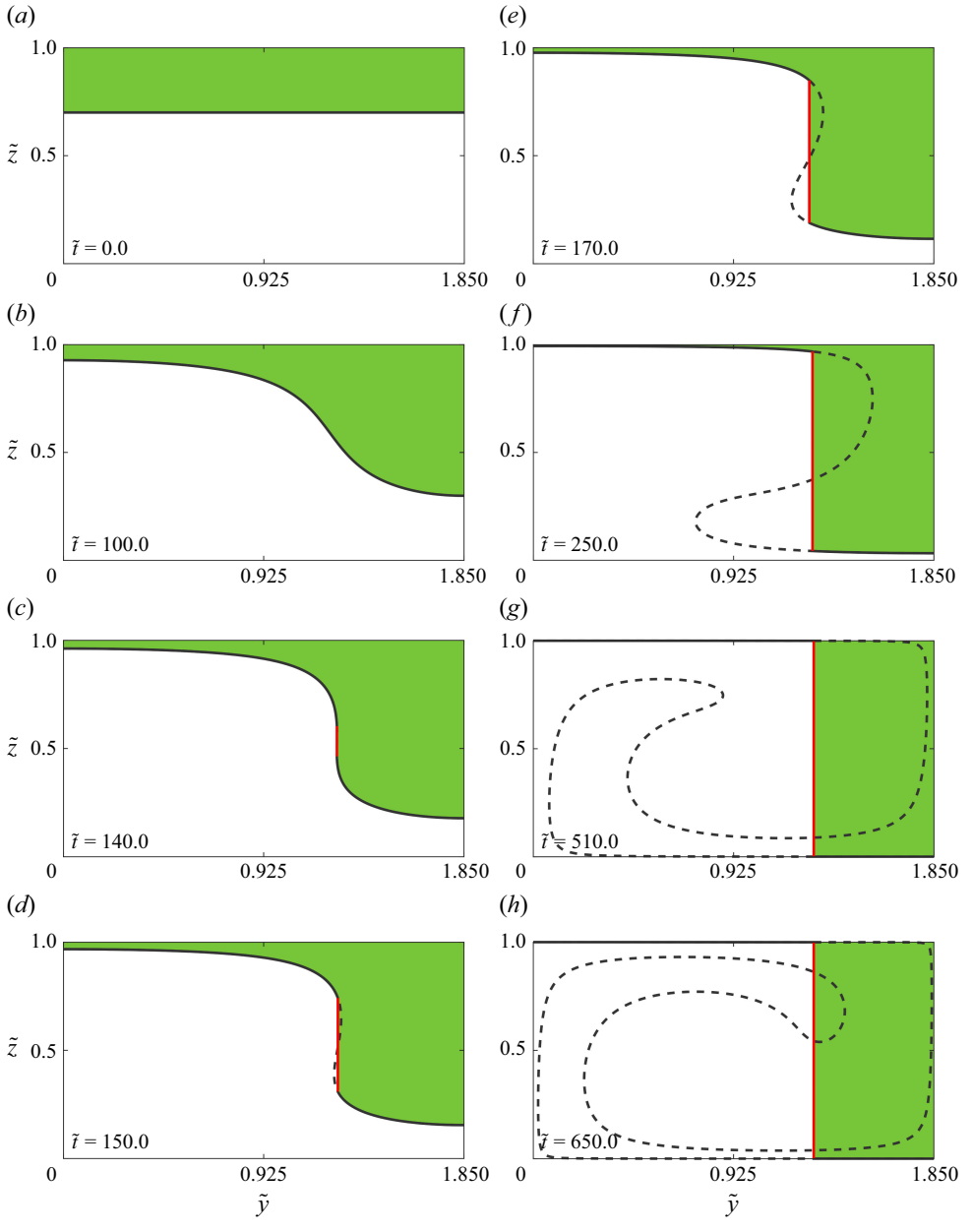


Figure 8. Comparison of the one-dimensional interface height $\tilde{\eta}$ (black line) calculated using the method of characteristics, and the full two-dimensional solution for ϕ^s in a single clockwise-rotating vortex cell, with the velocity field (2.21)–(2.22), and for a 30 : 70 mix and $(Pe,\ \Lambda) = (\infty,\ 100)$. The solutions are shown at (*a*) $\tilde{t} = 0$, (*b*) $\tilde{t} = 100$, (*c*) when the shock (red line) first forms at $\tilde{t} = 140$, (*d*) $\tilde{t} = 150$, (*e*) $\tilde{t} = 170$, (*f*) $\tilde{t} = 250$, (*g*) steady state $\tilde{t} = 510$ and (*h*) when the lobes cross the fitted shock as they continue to be swept round after steady state, $\tilde{t} = 650$. After the shock has formed the lobes of the interface are shown as dashed lines. Movie 6 shows the complete time-dependent solution.

https://doi.org/10.1017/jfm.2026.12176

6. Experimental development of the stripes along the chute

To investigate the formation of longitudinal stripes, and the downslope length scale over which they develop, experiments are performed on a straight 2.84 m long chute with glass sidewalls, spaced 7.8 cm apart, which is inclined at $\zeta = 34.5°$ to the horizontal. The chute's base is roughened with 750−1000 μm turquoise glass ballotini that is stuck down with double-sided tape. A 30 : 70 mixture of large green (200−250 μm) and small white (60−150 μm) glass ballotini is used. All the grains have the same intrinsic density. At the start of the chute, a hopper sits behind a two-gate system and is filled with a well-mixed sample. The first gate is set at 10 mm to maintain a steady inflow, and the second gate is lifted to initiate the flow. A tape measure is attached to the left-hand side of the chute, so that the downstream distance can easily be determined.

Movie 7 shows the time-dependent development of the flow. Approximately 8 s after the gate is opened a steady fully developed state develops along the chute as shown in figure 9. At steady state, material enters the chute with an evenly distributed green surface layer. White bands develop adjacent to the sidewalls after approximately 0.4 m, and become progressively wider with downstream distance, until reaching a constant width approximately 1 m downstream. Two large green bands, also develop, immediately adjacent to the white sidewall bands, while the central mixture still appears green at the surface (figure 9*a*). Once formed, the sidewall stripes continue downstream until the flow leaves the chute at 2.84 m. From $x = 1$ to approximately 2.3 m, four central large green bands slowly develop, and sharpen with increasing downstream distance, producing a total of six large green bands in the chute. The white bands at the sides of the flow are slightly wider than those in the centre of the channel (figure 9*b*,*c*). This fully developed steady-state segregation pattern persists until it reaches the end of the chute, where material freely falls into a container below.

Movie 7 also reveals a number of other interesting features. Firstly, at approximately 4 s after release the stripes can be seen to form immediately behind the front, 80 cm downstream of the gate. As Pearse *et al.* (2026) showed, the flow near the front is thinner in this transient phase, and has many more stripes than the steady state. These progressively coarsen as the flow thickens and are advected downstream and out of the chute. This suggests that the secondary motion develops rapidly, and responds dynamically to changes in flow height. The movie also shows that the striped pattern is not perfectly steady, and the stripes drift laterally backwards and forwards a small amount. The particles also segregate in the hopper, so towards the end of the experiment the inflow composition becomes richer in finer white grains and the green stripes in the chute become thinner although their position is still roughly the same. As the hopper runs out of material, the flow thickness progressively decreases, and the flow initially breaks down into a series of bidisperse roll waves (Viroulet *et al.* 2018), which are then superseded by a series of erosion–deposition waves (Edwards & Gray 2015), which have stationary material between the wave crests.

In view of the conceptual picture in figure 2, the formation of six large green bands suggests that a total of twelve counter-rotating vortex cells rapidly develop in the steady-state flow and align with the downslope direction. At each sidewall, where the white bands form, it is expected that the flow will be upwelling, and then there will be cross-slope motion at the surface towards the centre of the chute. Figure 10 shows a still image of the surface stripes and measurements of the surface velocities that were captured using a high-speed camera and calculated using the PIVLab package (Thielicke & Stamhuis 2014). The photo and measurements were made between 2.45 and 2.46 m down slope, and averaged over 1 s during the steady-state flow. The approximate downslope surface velocity in the centre of the chute $u^s_{centre} = 1.22\,\mathrm{m\,s^{-1}}$. However, figure 10 shows that the

https://doi.org/10.1017/jfm.2026.12176

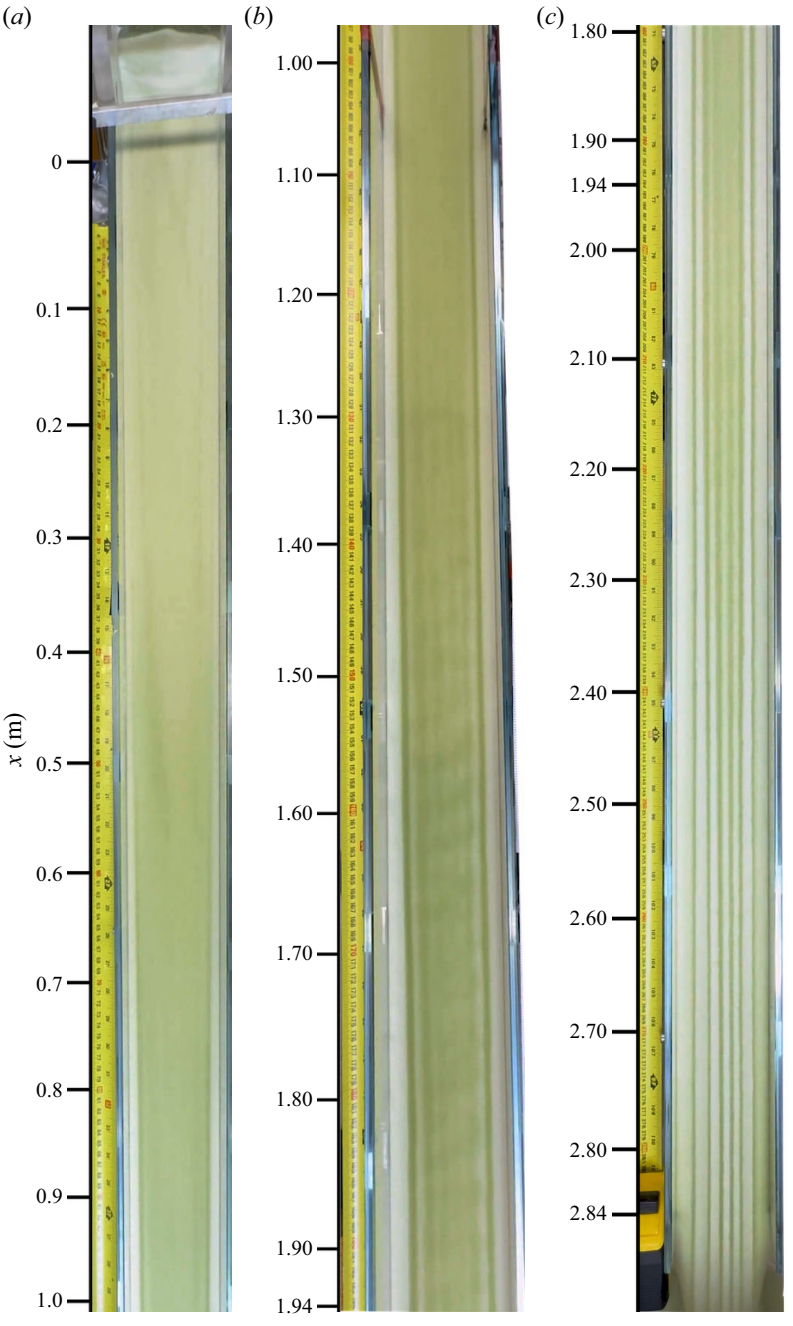


Figure 9. Overhead photographs at $t = 8$ s after release, showing the downstream development of a striped segregation pattern on a chute inclined at $\zeta = 34.5°$ to the horizontal. Three photographs span the full chute length with (*a*) showing the inflow gate and the flow from 0 to 1 m downstream, (*b*) the flow from 1 to 1.94 m and (*c*) the flow from 1.8 to 2.84 m as well as the free-flowing outflow. Each image is accompanied by a downstream distance measure in metres. This scale is based off the measuring tape attached to the left-hand side of the chute during experiments, and so takes into account the camera perspective. The flow consists of a 30 : 70 mix of large green (200−250 μm) and small white (60−150 μm) glass ballotini of the same intrinsic density. The full time-dependent experiment is shown in movie 7.

https://doi.org/10.1017/jfm.2026.12176

large-particle-rich green bands are moving approximately $0.2\,\mathrm{m\,s^{-1}}$ faster downslope than the fines-rich white bands, which is consistent with the dense flow regime of Börzsönyi *et al.* (2009). The variations in the velocity are less pronounced on the right of the chute, where the flow moves slightly slower. There are boundary layers of width $W_{BL} \simeq 14\,\mathrm{mm}$ adjacent to each sidewall, and the downslope surface velocity along the sidewall is $u^s_{wall} = 0.47\,\mathrm{m\,s^{-1}}$.

For steadily propagating flows, the front speed provides an indirect measure of the depth-averaged velocity $\bar{u}$ (Pouliquen 1999). It follows from the space–time plot in figure 10(*e*) that the depth-averaged downslope velocity in the centre of the channel

$$\bar{u}_{centre} \simeq 0.9584\,\mathrm{m\,s^{-1}}. \tag{6.1}$$

The downslope velocity was also observed through a transparent basal section of the chute. These observations showed that there was strong slip, which is consistent with a high-speed flow that forms a Leidenfrost basal layer (Wang *et al.* 2025).

The total half-width of the chute is $y_{wall} = 39\,\mathrm{mm}$. In order to fit in the remaining ten secondary vortices in the chute, they must be of average width $W = 5\,\mathrm{mm}$. The flow height during the steady phase is approximately 2.7 mm (Pearse *et al.* 2026), so the width to height aspect ratio of each secondary vortex in the centre of the channel is 1.85, which is the same as that assumed in the simulations in figures 2–8. The boundary layers at the side have a larger width to height ratio of 5.18, and the flow overall has a ratio of 28.89. The downslope surface velocity is used in § 7 to model the development of the stripes down the chute. Here, it is approximated using a simple function, which neglects the variations in surface velocity due to the formation of the subtle ridges and troughs. Figure 10(*d*) shows a comparison between the measured and fitted downslope surface velocity profiles. The experimental parameters are summarised in table 1. The cross-slope surface velocity is much harder to measure, because its magnitude is much smaller than the downstream velocity (Börzsönyi *et al.* 2009). Our attempts to measure it suggest that it is broadly consistent with the existence of twelve counter-rotating vortices, but there is too much drift in the data for it to be useful in determining the rotation rate of the cells.

7. Modelling the spatial development of the stripes along the chute

The experiments in § 6 show that it takes approximately $L = 2.3\,\mathrm{m}$ for the stripes to fully form in the centre of the channel, from a well-mixed inflow. However, at the sides of the flow, where lower velocity boundary layers are formed, a wide stripe of upwelling small particles develops after approximately 1 m. This section seeks to model this effect with the two-dimensional depth-averaged model developed in § 4, which assumes that ϕ^s is no longer spatially uniform in the downslope direction.

7.1. *A two-dimensional depth-averaged segregation model*

For simplicity, it is assumed that the flow is of constant depth H, is sharply inversely graded, with the particle-size distribution given by (5.2), and hence $H\overline{\phi^s} = \eta$, just as in (5.3) of the one-dimensional model developed in § 5.1. If the diffusion coefficient is also constant, then (4.4) reduces to

$$\frac{\partial \eta}{\partial t} + \frac{\partial}{\partial x}(H\overline{\phi^s u}) + \frac{\partial}{\partial y}(H\overline{\phi^s v}) = \frac{\partial}{\partial x}\left(D\frac{\partial \eta}{\partial x}\right) + \frac{\partial}{\partial y}\left(D\frac{\partial \eta}{\partial y}\right). \tag{7.1}$$

https://doi.org/10.1017/jfm.2026.12176

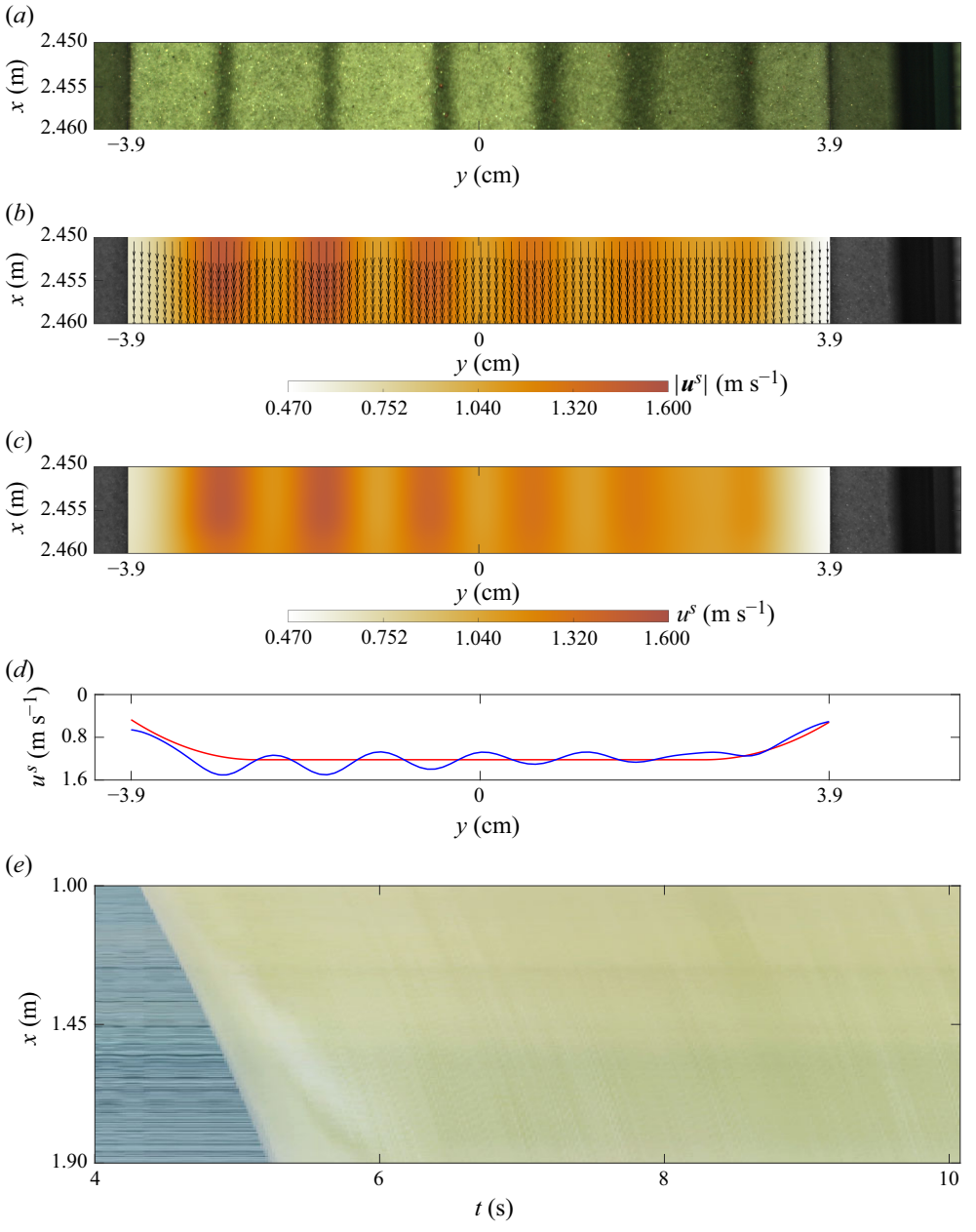


Figure 10. (*a*) Photo of the experiment on the straight chute showing the steady-state surface stripes of large green (200−250 μm) and small white (60−150 μm) particles on an incline of $\zeta = 34.5°$. The stripes are oriented in the downslope direction. Experimental measurements of (*b*) the surface velocity magnitude $|\boldsymbol{u}^s|$ and (*c*) the downslope surface velocity u^s. The relevant contour scales are shown below each plot. (*d*) A comparison of the measured downslope surface velocity across the chute at $x = 2.455$ m (blue line) and the simplified downslope surface velocity profile (7.10) used in numerical simulations (red line) with parameters $u^s_{centre} = 1.22\,\mathrm{m\,s^{-1}}$, $u^s_{wall} = 0.47\,\mathrm{m\,s^{-1}}$, $y_{wall} = 3.9$ cm and $y_{BL} = 2.5$ cm. This implies the width of the boundary layers is $W_{BL} = 14$ mm. The velocity measurements are calculated using the PIVLab package (Thielicke & Stamhuis 2014), and averaged over 1 s of flow data. (*e*) Space–time plot showing the propagation speed of the front. It is created by extracting a central column of pixels from each frame of movie 7 at 1–1.9 m downstream and stacking them next to each other.

https://doi.org/10.1017/jfm.2026.12176

$$y_{wall} = 39\,\text{mm},\ y_{BL} = 2.5\,\text{cm},\ H = 2.7\,\text{mm},\ W = 5\,\text{mm},\ L = 2.3\,\text{m},\ \zeta = 34.5^\circ$$
$$u^s_{centre} = 1.22\,\text{m}\,\text{s}^{-1},\ u^s_{wall} = 0.47\,\text{m}\,\text{s}^{-1},\ \bar{u}_{centre} \simeq 0.9584\,\text{m}\,\text{s}^{-1},\ \alpha = 0.727,$$
$$W_{BL} = 14\,\text{mm},\ \Omega = 1.389\,\text{s}^{-1},\ \Omega_{BL} = 3.8892\,\text{s}^{-1},$$
$$d^s = 1.05 \times 10^{-4}\,\text{m},\ d^l = 2.25 \times 10^{-4}\,\text{m},\ \phi^s = 0.7,\ \phi^l = 0.3,\ R = 2.1429,\ \Phi = 0.5,$$
$$\mathcal{A} = 0.108,\ \mathcal{B} = 0.7125,\ \mathcal{C} = 0.2712,\ \mathcal{E} = 2.0957,$$
$$q = 0.0076\,\text{m}\,\text{s}^{-1},\ D = 4.1607 \times 10^{-7}\,\text{m}^2\,\text{s}^{-1},$$
$$Pe = 49.04,\ \Lambda = 2.0155,\ \Xi = 14.3455.$$

Table 1. Top row: approximate experimental parameters for the striped chute flow shown in figure 10. Second row: parameters for the fitted surface velocity profile and velocity reconstruction. Third row: width of the sidewall boundary layer and assumed rotation rates of the secondary vortices. Fourth row: experimental particle sizes, average large- and small-particle concentrations and the particle-size ratio. The value of the solids volume fraction Φ is based on an averaged value in the DEM simulations of Börzsönyi *et al.* (2009). Fifth row: universal constants used in Trewhela *et al.*'s (2021) experimental scaling law for the segregation rate and the generalised form of Utter & Behringer's (2004) diffusivity. The value of $\mathcal{B}$ differs from that of Trewhela *et al.* (2021), and accounts for the absence of interstitial fluid (Maguire *et al.* 2024). Sixth row: the resultant constant segregation velocity q and diffusion coefficient D based on evaluating Trewhela *et al.*'s (2021) segregation law at $z = H/2$ and assuming linear shear through the flow depth. Seventh row: the final non-dimensional numbers for the experimental flow.

This is subject to an initial condition

$$\eta(x, y, t) = \eta_0(x, y), \quad \text{for} \quad (x, y) \in [0, \mathscr{L}] \times [-y_{wall}, y_{wall}], \tag{7.2}$$

where $\mathscr{L}$ is the length of the chute and the sidewalls are located at $y = \pm y_{wall}$. At the inflow ($x = 0$), a constant interface height η_o is prescribed across the chute

$$\eta(0, y, t) = \eta_o, \quad \text{in} \quad y \in [-y_{wall}, y_{wall}], \tag{7.3}$$

and along the sidewalls the no-flux condition implies that

$$\frac{\partial \eta}{\partial y} = 0, \quad \text{at} \quad y = \pm y_{wall}. \tag{7.4}$$

The grains are allowed to freely flow out of the chute at $x = \mathscr{L}$, which is equivalent to the condition

$$\frac{\partial \eta}{\partial x} = 0, \quad \text{at} \quad x = \mathscr{L}. \tag{7.5}$$

In order to close the model, it remains to determine expressions for the depth-averaged flux of small particles in the downslope and cross-slope directions.

7.2. *The downslope velocity profile and flux function*

Following Gray & Kokelaar (2010*a*,*b*), a simple linear velocity profile is prescribed for the downslope velocity through the depth of the flow, i.e.

$$u = \overline{u}\left(\alpha + 2(1-\alpha)\frac{z}{H}\right), \tag{7.6}$$

where the depth-averaged downslope velocity $\overline{u} = \overline{u}(y)$ is still able to vary across the channel. This should be viewed as a first-order Taylor series approximation to the true velocity profile. The parameter $\alpha \in [0, 1]$ sets the amount of shear through the avalanche depth, with $\alpha = 1$ corresponding to plug flow and $\alpha = 0$ representing simple shear. In the centre of the channel, (7.6) implies that the downslope surface and depth-averaged

https://doi.org/10.1017/jfm.2026.12176

velocities, u^s_{centre} and $\bar{u}_{centre}$, are related by the formula

$$u^s_{centre} = \overline{u}_{centre}(2-\alpha), \tag{7.7}$$

which can be used to infer the value of

$$\alpha = 2 - \frac{u^s_{centre}}{\bar{u}_{centre}} \simeq 0.727 \tag{7.8}$$

from the experimental measurements in § 6. This value of α implies that there is shear through the flow depth as well as a significant amount of basal slip, which is consistent with the formation of a low solids volume fraction basal Leidenfrost layer (Wang *et al.* 2025).

Substituting the downstream velocity profile (7.6) into the integral for the downstream flux of small particles (4.3*b*) implies that

$$H\overline{\phi^s u} = \overline{u}\left(\eta - (1-\alpha)\left(\eta - \frac{\eta^2}{H}\right)\right). \tag{7.9}$$

Despite its simplicity, the downslope velocity profile (7.6) and the associated downslope flux of small particles (7.9) capture many essential features of the flow, and have been used to model the accumulation of large particles at avalanche fronts, as well as segregation-induced flow fingering in fully coupled depth-averaged models (Gray & Kokelaar 2010*a*,*b*; Woodhouse *et al.* 2012; Baker *et al.* 2016).

The experimental measurements of the surface velocity, shown in figure 10, suggest that the sides of the flow move slower than the centre. To parameterise this, the downslope surface velocity is assumed to take the form

$$u^s(y) = \begin{cases} u^s_{centre} + (u^s_{wall} - u^s_{centre})\left(\dfrac{y + y_{BL}}{-y_{wall} + y_{BL}}\right)^2, & -y_{wall} \leqslant y < -y_{BL}, \\ u^s_{centre}, & -y_{BL} \leqslant y \leqslant y_{BL}, \\ u^s_{centre} + (u^s_{wall} - u^s_{centre})\left(\dfrac{y - y_{BL}}{y_{wall} - y_{BL}}\right)^2, & y_{BL} < y \leqslant y_{wall}, \end{cases} \tag{7.10}$$

where the surface wall-slip velocity is equal to u^s_{wall} at $y = \pm y_{wall}$ and the central plug of material moves downslope with constant surface velocity u^s_{centre}. The flow is symmetric about $y = 0$ and has two boundary layers that smoothly connect to the central velocity at $y = \pm y_{BL}$. This approximation is illustrated in figure 10(*d*) for the case $y_{BL} = 5W$. It neglects the subtle variations in the downslope surface velocity across the slope, which correlate with the flow bands/ridges, but is a reasonable first approximation. The reconstructed two-dimensional downslope velocity field u is shown using dimensional variables in figure 11(*b*).

7.3. *The cross-slope flux function*

Figure 10 shows that the sidewall boundary layers have an upwelling band of fines-rich material immediately adjacent to the wall, and that the ends of the boundary layers are approximately at the centre of the first large–rich band. Moreover, in the centre of the flow, where the downslope surface velocity is plug-like, there are five complete stripes measured from centre to centre of each large–rich band. This implies that in the centre of the flow there must be ten counter-rotating secondary vortices, which are flanked on either side by a wider secondary vortex in each wall boundary layer. The cross-slope velocity field can

https://doi.org/10.1017/jfm.2026.12176

https://doi.org/10.1017/jfm.2026.12176

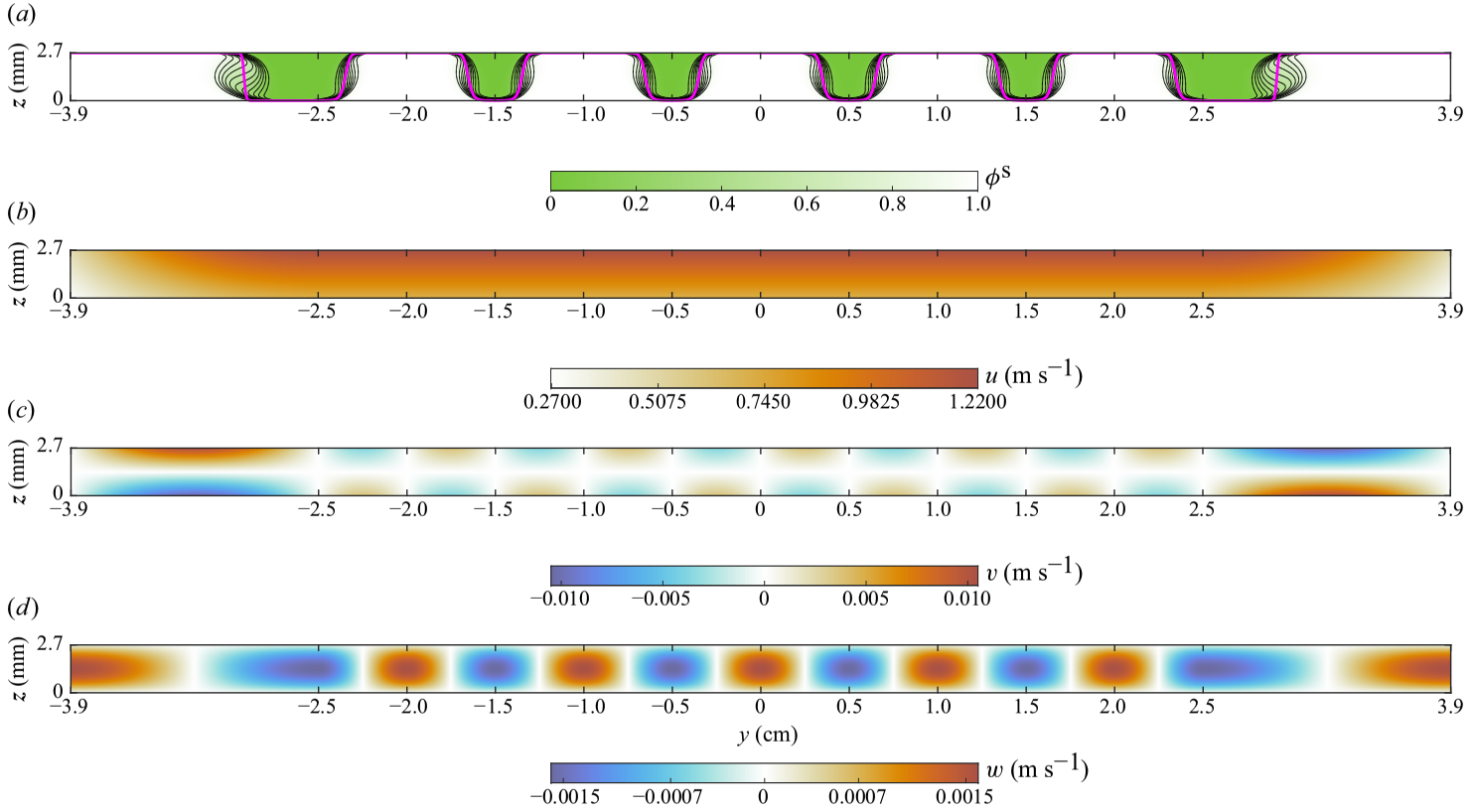


Figure 11. (*a*) Comparison between the two-dimensional steady-state solution for the small-particle concentration $\phi^s(y, z)$ (contour plot) and the one-dimensional depth-averaged model interface height $\eta(y)$ (magenta line) at $t = 10$ s for the experimental parameters in table 1. This is equivalent to the case $(Pe, \Lambda) = (49.04, 2.0155)$. The two solutions are computed with a prescribed velocity field $\boldsymbol{u}(y, z)$, which is independent of the downslope coordinate x. Panels (*b*, *c*, *d*) show contour plots of the downslope, cross-slope and slope-normal velocity components (u, v, w), respectively. The contour lines in (*a*) are shown in the range $\phi^s \in [0.1, 0.9]$ in 0.08 increments.

therefore be parameterised by

$$v = \begin{cases} -\Omega_{BL} \sin\left(\dfrac{\pi}{W_{BL}}(y+5W)\right)(2z-H), & -y_{wall} \leqslant y < -5W, \\ \Omega \sin\left(\dfrac{\pi y}{W}\right)(2z-H), & -5W \leqslant y \leqslant 5W, \\ -\Omega_{BL} \sin\left(\dfrac{\pi}{W_{BL}}(y-5W)\right)(2z-H), & 5W < y \leqslant y_{wall}, \end{cases} \tag{7.11}$$

where W_{BL} is the width of the sidewall boundary layer and Ω_{BL} is its rotation rate. Note that the prescribed cross-slope velocity in the central channel is exactly the same as in (2.12). The cross-slope velocity in the two boundary layers has a similar functional form, but is implicitly assumed to rotate in the opposite direction to the adjacent cell (hence the minus sign). The experiments in § 6 suggest that the edge of the downslope velocity boundary layers is the same as the edge of the (wider) sidewall secondary vortices, i.e. that

$$y_{BL} = 5W, \tag{7.12}$$

and hence the width of the boundary layer is

$$W_{BL} = y_{wall} - 5W. \tag{7.13}$$

In order to determine Ω_{BL} it is necessary to consider the slope-normal velocity w. Since the velocity field is incompressible and satisfies (2.9), the normal velocity can be reconstructed by differentiating (7.11) with respect to y and integrating with respect to z, subject to the boundary condition that $w = 0$ at $z = 0$, to give

$$w = \begin{cases} \dfrac{\Omega_{BL}\pi}{W_{BL}} \cos\left(\dfrac{\pi}{W_{BL}}(y+5W)\right) z(z-H), & -y_{wall} \leqslant y < -5W, \\ -\dfrac{\Omega\pi}{W} \cos\left(\dfrac{\pi y}{W}\right) z(z-H), & -5W \leqslant y \leqslant 5W, \\ \dfrac{\Omega_{BL}\pi}{W_{BL}} \cos\left(\dfrac{\pi}{W_{BL}}(y-5W)\right) z(z-H), & 5W < y \leqslant y_{wall}. \end{cases} \tag{7.14}$$

The normal velocity w must vary smoothly across the interfaces between the boundary layers and the central region. Evaluating (7.14) at $y = \pm 5W$ it follows that the counter-rotating vortices in the boundary layers are consistent with those in the central flow, provided

$$\Omega_{BL} = \left(\frac{W_{BL}}{W}\right) \Omega. \tag{7.15}$$

Since the boundary layers are wider than the secondary vortices in the central part of the flow, they must rotate faster to be compatible (i.e. to prevent a contact discontinuity in w forming at $y = \pm 5W$). The components of the reconstructed velocity field are shown in figure 11.

https://doi.org/10.1017/jfm.2026.12176

Finally, multiplying the cross-slope velocity (7.11) by the small-particle concentration (5.2) and integrating through the depth, implies that the cross-slope flux function is

$$H\overline{\phi^s v} = \begin{cases} -\Omega_{BL} \sin\left(\dfrac{\pi}{W_{BL}}(y+5W)\right)(\eta^2 - H\eta), & -y_{wall} \leqslant y < -5W, \\ \Omega \sin\left(\dfrac{\pi y}{W}\right)(\eta^2 - H\eta), & -5W \leqslant y \leqslant 5W, \\ -\Omega_{BL} \sin\left(\dfrac{\pi}{W_{BL}}(y-5W)\right)(\eta^2 - H\eta), & 5W < y \leqslant y_{wall}. \end{cases} \tag{7.16}$$

Note that, in the centre of the flow, (7.16) is identical to the cross-slope flux function (5.4) derived in § 5. Before using the two-dimensional depth-averaged theory (7.1) to model the stripe formation down the chute, it is instructive to compute the depth-averaged solution in the chute geometry shown in figure 11 assuming spatial uniformity in the downslope direction x, and to compare it against the two-dimensional non-depth-averaged theory of § 2. Both theories still need a number of experimental parameters to be determined.

7.4. *Experimental parameter estimation*

In order to solve the full segregation-advection-diffusion equation (2.10), the segregation rate q and the diffusivity D are approximated using the experimental scaling laws of Utter & Behringer (2004) and Trewhela *et al.* (2021). In its generalised form, Utter & Behringer's (2004) law implies that

$$D = \mathcal{A}\dot{\gamma}\bar{d}^2, \tag{7.17}$$

where $\mathcal{A}$ is a universal constant specified in table 1, $\dot{\gamma}$ is the shear rate and $\bar{d}$ is the average local particle size. The downslope flow is much larger than the secondary flow, so to leading order the shear rate

$$\dot{\gamma} = \left|\frac{\partial u}{\partial z}\right| = 2(1-\alpha)\frac{\bar{u}}{H}, \tag{7.18}$$

which is constant through the flow depth, provided the linear downslope velocity profile (7.6) is assumed. The constant α is determined in (7.8). The average local particle size

$$\bar{d} = \phi^l d^l + \phi^s d^s, \tag{7.19}$$

where d^l and d^s are the diameters of the large and small particles, respectively. This is approximated using the values of the particle diameters and concentrations given in table 1. It follows that the diffusivity in the central channel is approximately equal to

$$D = 4.1607 \times 10^{-7}\ \mathrm{m^2\ s^{-1}}. \tag{7.20}$$

In the simulations this constant value is assumed throughout the entire flow, even in the sidewall boundary layers, where the shear rate and slip may be modified.

Trewhela *et al.*'s (2021) experimental scaling law for the segregation rate

$$q = \frac{\mathcal{B}\dot{\gamma}\bar{d}^2\mathcal{F}}{\mathcal{C}\bar{d} + \Phi(H-z)}, \tag{7.21}$$

captures the observed shear-rate and pressure dependence through the flow depth, as well as the particle-size ratio $R = d^l/d^s$ dependence in the factor

$$\mathcal{F} = (R-1) + \mathcal{E}\phi^l(R-1)^2. \tag{7.22}$$

https://doi.org/10.1017/jfm.2026.12176

In this law $\mathcal{B}$, $\mathcal{C}$ and $\mathcal{E}$ are universal constants that are given in table 1. In order to find a representative constant value for q, the scaling law is evaluated at $z = H/2$ and $\bar{d}$ is approximated by a global average (as above). Substituting the values given in table 1 implies that the segregation velocity

$$q = 0.0076\,\mathrm{m\,s^{-1}}. \tag{7.23}$$

The large and small particles are therefore able to segregate from one another at a maximum velocity of $7.6\,\mathrm{mm\,s^{-1}}$. This is quite fast, but is a consequence of the thinness of the flow.

Measuring the cross-slope surface velocity is difficult, because it is so much smaller than the downslope velocity. However, it is possible to use the depth-averaged segregation equation (7.1) to infer an approximate value. At steady state, the dominant balance is between the downslope flux gradient and the cross-slope flux gradient

$$\frac{\partial}{\partial x}(H\overline{\phi^s u}) \sim \frac{\partial}{\partial y}(H\overline{\phi^s v}). \tag{7.24}$$

The experiments in § 6 suggest that order-unity changes in the downslope direction occur on a length scale $L = 2.3$ m, but order-unity changes across the slope are of the same order as the flow depth H. Moreover, assuming that the downslope flux $H\overline{\phi^s u}$ in (7.9) can be approximated by $\bar{u}\eta$ and the cross-stream flux $H\overline{\phi^s v}$ in (7.16) by $\Omega(H\eta - \eta^2)$, then (7.24) implies that

$$\frac{\bar{u}\eta}{L} \sim \frac{\Omega(H\eta - \eta^2)}{H}, \quad \Rightarrow \quad \Omega \sim \frac{\bar{u}H}{L(H-\eta)}. \tag{7.25a,b}$$

Substituting the measured value of $\bar{u}$ from (6.1) and assuming that the interface lies at approximately $\eta = 0.7H$ then it follows from (7.25*b*) that the rotation rate in the centre of the channel is approximately

$$\Omega = 1.389\,\mathrm{s^{-1}}. \tag{7.26}$$

This implies that maximum surface cross-slope velocities are of the order of $\Omega H \sim 3.8\,\mathrm{mm\,s^{-1}}$. It follows from (7.15) that the faster rotation rate of the secondary vortices in the sidewall boundary layers is

$$\Omega_{BL} = 3.8892\,\mathrm{s^{-1}}, \tag{7.27}$$

implying a maximum surface velocity of $10.5\,\mathrm{mm\,s^{-1}}$. This is consistent with the bi-disperse roll wave experiments of Viroulet *et al.* (2018), where fines-rich boundary layers also formed. In particular, Viroulet *et al.*'s (2018) movie 1 shows that, as each large–rich roll wave front overtakes the material in front of it, large particles are pushed towards the sidewall, but are then advected back towards the centre of the channel prior to the arrival of the next wave. Finally, using their definitions (2.17*a*,*b*) and (5.14) the non-dimensional parameters are

$$Pe = 49.04, \quad \Lambda = 2.0155, \quad \Xi = 14.3455. \tag{7.28}$$

All the dimensional and non-dimensional numbers needed to simulate the experimental flow, in both the depth-averaged and non-depth-averaged models, are summarised in table 1.

https://doi.org/10.1017/jfm.2026.12176

7.5. *Comparison between the one- and two-dimensional representations of the experiment*

In this section the particle-size distribution is assumed to be spatially uniform in the downslope direction. It follows that the depth-averaged model reduces to a one-dimensional problem across the chute, while the non-depth-averaged theory reduces to a two-dimensional problem in a $(\tilde{y}, \tilde{z})$ section. The flow is assumed to be initially sharply segregated in an inversely graded configuration (large particles above small ones) with an interface located at

$$\eta_0(y) = 0.7H. \tag{7.29}$$

This is equivalent to an initial particle-size distribution of the form

$$\phi_0^s(y) = \begin{cases} 0, & z > 0.7H, \\ 1, & z \leqslant 0.7H, \end{cases} \tag{7.30}$$

to again reflect the 30 : 70 mix of large (green) and small (white) particles used in the experiment. The solutions are computed in dimensional variables to ensure that they can easily be compared with the experimental observations. The results are shown in figure 12 and movie 8. Focusing first on the two-dimensional theory, at $t = 0.5$ s the interface between large and small particles is still very sharp, but it has been rotated by the secondary flow to create a wavy interface. The large particles concentrate in the downwelling sections and small particles concentrate in the upwelling sections. The amplitude of the wavy interface grows with increasing time, with parts of the interface becoming progressively steeper until they break at $t \simeq 1$ s to form a series of small diffuse breaking-size-segregation waves (Thornton & Gray 2008; Gray & Ancey 2009; Edwards *et al.* 2023). These grow in height and width until they occupy the whole depth of the flow, and white stripes of small particles become visible at the surface at $t \simeq 1.5$ s. The breaking-size-segregation waves in the boundary layers are larger and wider than those in the centre of the flow, which is a consequence of the increased rotation rate Ω_{BL} of the secondary vortices. The central diffuse breaking waves rapidly attain a steady state, as shown in movie 8. However, the diffusion is not strong enough to immediately damp out the oscillation of the larger breaking waves in the sidewall boundary layers, and they oscillate for some time. A total of six stripes develop across the chute, reflecting the underlying secondary flow, and in agreement with the experimental results in figures 9 and 10. The stripes adjacent to the sidewall boundary layers are wider than those in the central channel, which matches the observations in figure 9(*b*). Throughout the entire time-dependent evolution, the one-dimensional depth-averaged theory agrees remarkably well with the interface position predicted by the full theory. The depth-averaged model cannot capture the structure of the diffuse breaking-size-segregation waves, but instead represents them by a sharp transition that accurately picks off their approximate location. The depth-averaged theory therefore provides a very useful reduced representation of the much more complex two-dimensional small-particle concentration field, and has the advantage that it can be used to efficiently model the development of the stripes down the entire chute.

7.6. *Depth-averaged solutions for the stripe development along the chute*

The two-dimensional depth-averaged segregation equation (7.1), with the flux functions (7.9) and (7.16), is solved in the domain $(x, y) \in [0, 2.84\,\text{m}] \times [-y_{wall}, y_{wall}]$. The domain is initially filled with material of constant height H that is moving downslope and simultaneously undergoing secondary recirculation. The velocity field $\boldsymbol{u}$ is assumed to be steady and fully developed in the downstream direction, with velocity components

https://doi.org/10.1017/jfm.2026.12176

https://doi.org/10.1017/jfm.2026.12176

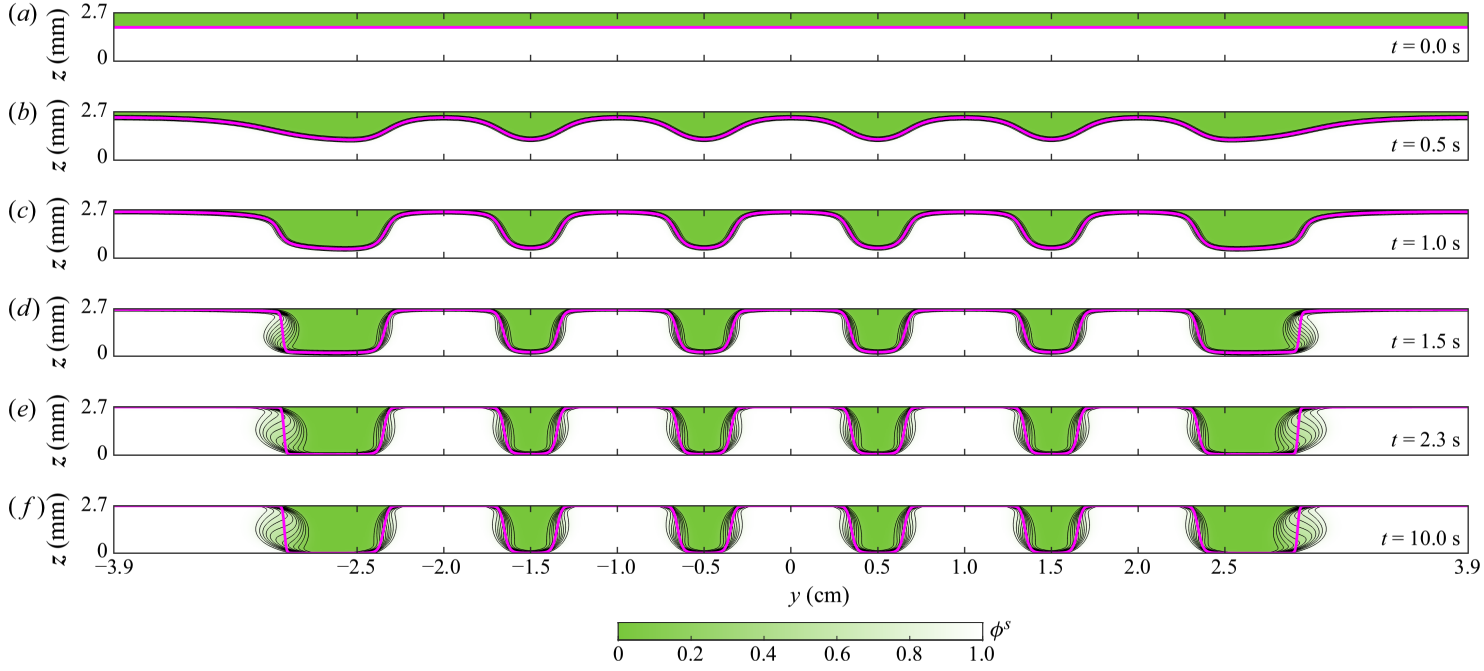


Figure 12. (*a–f*) Comparison between the two-dimensional time-dependent solutions for the small-particle concentration $\phi^s(y, z, t)$ (contour plot) and the one-dimensional depth-averaged model interface $\eta(y, t)$ (magenta line) at a sequence of times and for the experimental parameters in table 1. This is equivalent to the case $(Pe, \Lambda) = (49.04, 2.0155)$. The flow assumes ten central secondary vortices of width $W = 0.5$ cm and a boundary layer on either side with a vortex cell of width $W_{BL} = 1.4$ cm, as illustrated in figure 11. The boundaries of the secondary vortices are indicated by the tick marks along the y axis. Movie 8 shows an animation of the time-dependent evolution of the solution. The contour lines are shown in the range $\phi^s \in [0.1, 0.9]$ in 0.08 increments.

(u, v, w) given by (7.6), (7.11) and (7.14), respectively, and illustrated in figure 11. This is implicitly encoded in the flux functions (7.9) and (7.16).

Material is continuously supplied at the inflow at $x = 0$, and is assumed to be uniformly distributed across the chute. Since the inflow is implicitly assumed to be inversely graded, with all the large particles on top of the small ones, the small-particle layer needs to be thicker in order to transport the correct flux down the chute. Assuming the downslope velocity profile (7.6), the downslope small-particle flux

$$F^s = \int_0^H \phi^s u \, \mathrm{d}z = \overline{u} \left(\alpha\eta + (1-\alpha)\frac{\eta^2}{H} \right), \tag{7.31}$$

and the total flux

$$F = \int_0^H u \, \mathrm{d}z = H\overline{u}. \tag{7.32}$$

The correct proportion of small grains in the flowing mixture is achieved when the ratio of the small-particle flux F^s to the total flux F is equal to the concentration of the static mixture of grains ϕ^s_{static}, i.e. $F^s/F = \phi^s_{static}$. Substituting (7.31) and (7.32) into this expression yields the quadratic equation

$$(1-\alpha)\left(\frac{\eta}{H}\right)^2 + \alpha\left(\frac{\eta}{H}\right) - \phi^s_{static} = 0, \tag{7.33}$$

which can be solved to determine the corrected inflow height

$$\eta_0(y) = \left(\frac{-\alpha + \sqrt{\alpha^2 + 4(1-\alpha)\phi^s_{static}}}{2(1-\alpha)} \right) H. \tag{7.34}$$

For the 30 : 70 mix the static concentration $\phi^s_{static} = 0.7$. It follows that for the velocity profile (7.6) with α given by (7.8), the corrected inflow height is

$$\eta_0(y) = 0.751\, H, \tag{7.35}$$

which is only a 7 % correction, because the downslope velocity has a lot of basal slip. The material in the chute at $t = 0$ is also assumed to have the same initial interface height, i.e.

$$\eta_0(x, y) = 0.751\, H. \tag{7.36}$$

Note that the depth-averaged theory implicitly assumes that the bidisperse mixture is sharply inversely graded as it enters the chute. This may not be the case, despite some segregation probably occurring as the grains are sheared towards the hopper exit. However, balancing the downslope flux of small particles with the segregation term in (2.5) suggests that the dominant balance is

$$\frac{\partial}{\partial x}(\phi^s u) \sim \frac{\partial}{\partial z}\left(q\phi^s(1-\phi^s)\right). \tag{7.37}$$

If vertical gradients occur on the length scale of the flow depth $H = 0.0027$ m, a typical depth-averaged downslope velocity $\bar{u} = 0.9584\,\mathrm{m\,s^{-1}}$ and a typical segregation velocity $q = 0.0076\,\mathrm{m\,s^{-1}}$ then the approximate downslope distance L_{seg} for complete vertical segregation through the flow depth is

$$L_{seg} \sim \frac{H\bar{u}}{q} = 34\,\mathrm{cm}. \tag{7.38}$$

https://doi.org/10.1017/jfm.2026.12176

The segregation into inversely graded layers will therefore have occurred in the first 12 % of the chute, and may well have completed earlier if there is segregation prior to the grains exiting the hopper. Moreover, even if segregation is continuing to occur as the grains are flowing downslope, they are already being rotated by the secondary flow, so large and small particles will begin to concentrate in the downwelling and upwelling regions almost immediately.

Movie 9 shows a top down animated contour plot of the time-dependent solution along the chute, and the steady state is shown in figure 13. In these plots the colour bar is chosen to reflect what a viewer sees from above. Note that when there is more than a monolayer of large green particles at the experimental flow surface, the surface appears green, regardless of how deep the large–small-particle interface η lies beneath it. To approximate this effect, the colour bar is therefore skewed towards green. In particular, the gradient in the colour bar, from green to white, is chosen so that it occurs when the interface height η is within one large-particle diameter of the surface. It is also important to stress that in the experiment there is initially no material in the chute, so the time-dependent simulation and movie 7 are not directly comparable. However, the steady-state solution shown in figure 13 is comparable to figure 9.

Material entering the chute is a uniform shade of green, as in the experiments, and a white stripe begins to emerge adjacent to each sidewall at approximately $x = 0.5$ m. At this point the material in the centre of the channel still appears uniformly green. However, the reconstructed cross-section of the small particle-size distribution across the channel at $x = 0.5$ m, shown in figure 14(c), indicates that the secondary recirculation has already caused a wavy interface to form across the channel. This remains unseen both in the experiment and in the simulated top down view in figure 13. The white stripes adjacent to the sidewalls thicken with downstream distance and are approximately fully formed by 1.2 m downslope, after which they do not noticeably change width down the whole of the rest of the channel. All of this behaviour is in good agreement with the experiment, although the white stripes in the experiment appear to start to form slightly higher up the chute and reach their steady-state width somewhat earlier.

The first vestiges of the stripes that form in the central channel begin to emerge in the simulations at $x = 0.8 - 1.0$ m in figure 13(a). This is approximately the same distance that higher and lower concentrations of large and small particles are seen in the experiments. The cross-section at $x = 1$ m shows that the interface η is very close to the free surface in the fines-rich upwelling regions, but it has not fully penetrated through to the surface (figure 14e). Equally, in the large–rich downwelling sections, large particles have still not reached the base of the flow. By $x = 1.5$ m these thin layers become progressively thinner (see figure 14f) and the stripes become visible at the surface (figure 13b) in accordance with the experiment. A total of six large–rich bands then form in the channel, as a direct consequence of the twelve counter-rotating vortices across the width of the flow (figure 11) and in accordance with the conceptual picture in figure 2. With increasing downstream distance the bands sharpen up and achieve their steady-state width approximately 2.3 m downslope, as suggested by the scaling argument in (7.25).

Movie 10 shows an animation of the time-dependent development of the stripes in each of the cross-sections shown in figure 14. Each of these cross-sections looks a little like those illustrated in figure 12, but here they are cross-sections at a fixed time and a series of different locations, rather than being at a fixed location and at variable times. In addition, movie 10 looks considerably simpler than movie 8, because the depth-averaged theory cannot represent the structure of the breaking-size-segregation waves. Nevertheless this simplified reconstruction of the particle-size distribution from the depth-averaged model captures many essential features of the development of the stripes.

https://doi.org/10.1017/jfm.2026.12176

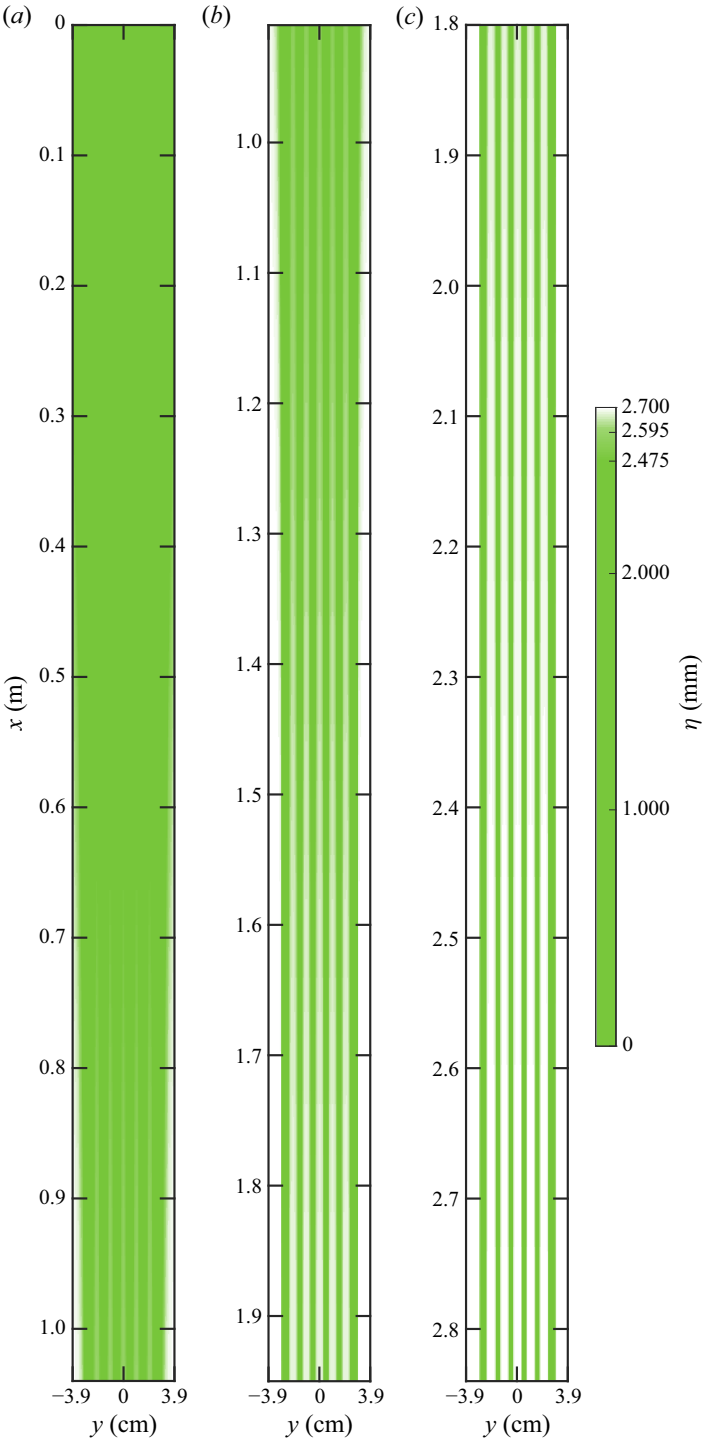


Figure 13. Contour plot showing the depth-averaged interface height $\eta(x, y)$ at $t = 8$ s for the experimental parameters in table 1 and the velocity field in figure 11. The simulation domain is split into three regions (*a*) 0–1.04 m, (*b*) 0.91–1.95 m and (*c*) 1.8–2.84 m consistent with experiments shown in figure 9. The colour bar is skewed to make the colours representative of surface observations in a real flow. A time-dependent movie of the simulation is shown in movie 9 and figure 14 shows a series of cross-sections across the chute.

https://doi.org/10.1017/jfm.2026.12176

https://doi.org/10.1017/jfm.2026.12176

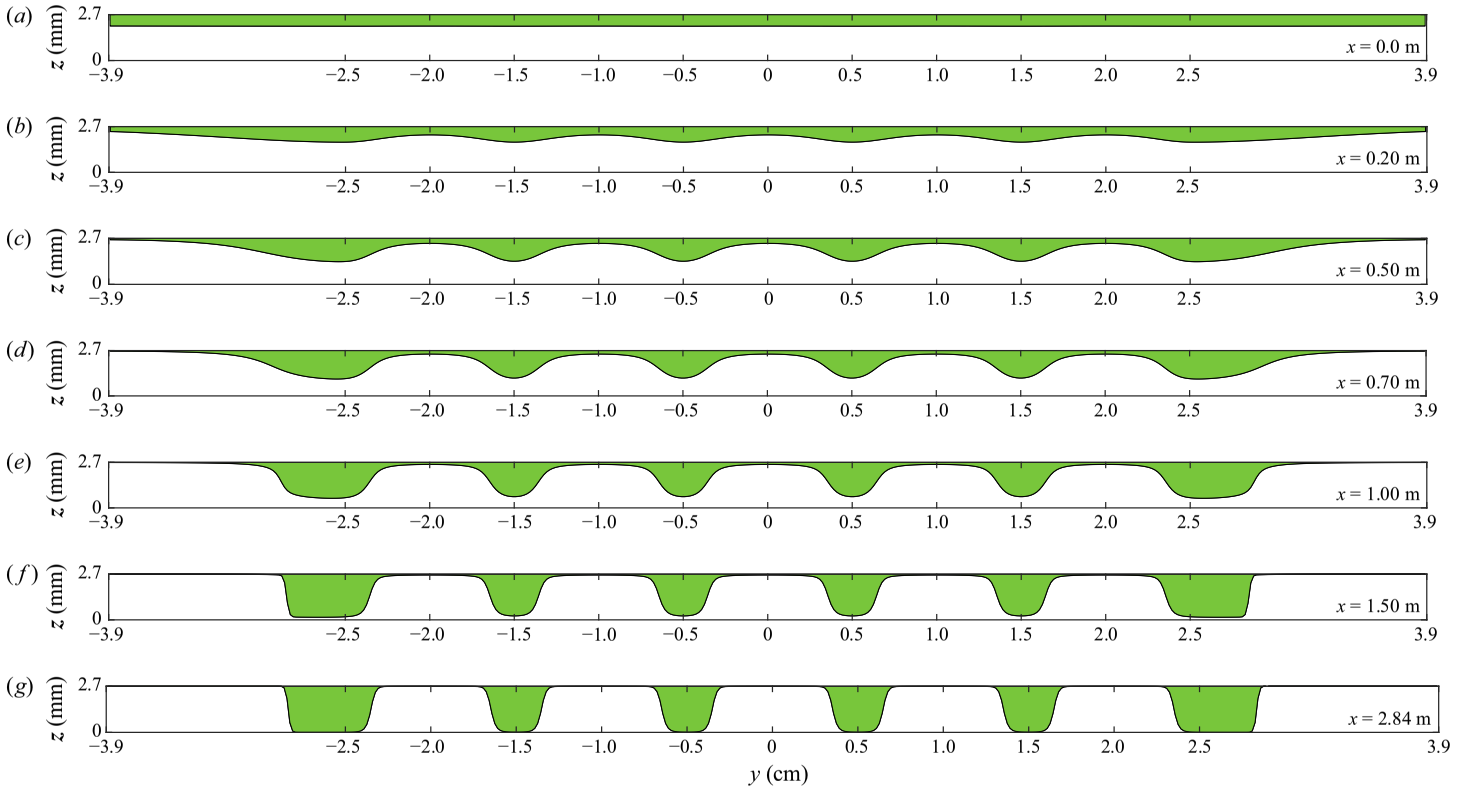


Figure 14. (*a–g*) A series of (y, z) sections reconstructed from the steady-state depth-averaged solution $\eta(x, y)$ at $t = 8$ s shown in figure 13 and computed with the experimental parameters in table 1. Each section shows the interface position $\eta(y)$, which lies along the interface between large particles (shaded green) and small particles (shaded white). The boundaries of the secondary vortices are indicated by the tick marks along the y axis. Movie 10 shows the time-dependent development of the solution in each cross-section.

In movie 10, the section at $x = 0.2$ m starts off with a horizontal interface (reflecting the inversely graded initial conditions) and starts to develop a series of waves. However, by $t = 0.2$ s the waves have already reached their maximum steady-state amplitude and do not develop further. In this wavy configuration the interface η never reaches the free surface, and so the surface of the flow will appear green in the experiments. At $x = 0.5$ m the waves become more pronounced and stop developing at approximately $t = 0.5$ s. At the sides of the flow the interface η is sufficiently close to the surface that the upwelling fine material becomes visible in the top down reconstruction in figure 13. In the centre of the channel, however, there is still no sign of the internal waviness in the surface view.

The sections at $x = 0.7$ and $x = 1$ m reach steady state in the centre of the channel at approximately $t = 0.7$ and $t = 1$ s, respectively, reflecting the fact that the depth-averaged downslope velocity $\bar{u}_{centre} \simeq 0.9584\,\mathrm{m\,s^{-1}}$ in the centre of the channel. Note that there is some continued evolution of the interface in the sidewall boundary layers after this time, because the downslope velocity is lower there. At $x = 1$ m the stripes start to become visible in the top down view, and they become progressively stronger with increasing downstream distance (see figure 13 and movie 9). At $x = 1.5$ and $x = 2.84$ m the initial evolution of the interface looks like that in the time-dependent movie of the spatially uniform problem in figure 12 and movie 8. This is because the initial condition (7.36) implies that the initial evolution is precisely uniform in the downslope direction x, and it is not until $t = 1.5$ and $t = 2.84$ s that the influence of the upstream boundary condition reaches these locations, respectively. Interestingly, after this time both profiles adjust slightly from the solutions that would be generated by a purely spatially uniform problem, as the lateral diffusion pushes some of the large grains that were initially in the sidewall vortices into the neighbouring internal vortex cells. Overall the depth-averaged model (7.1) does a remarkably good job of capturing both the qualitative and quantitative development of stripes observed in experiments in figure 9. In particular, it predicts the formation of alternating longitudinal bands of pure large and pure small particles that extend all the way through the flow depth. This is consistent with what Pearse *et al.* (2026) observed in the curved chute deposit, shown in their figure 3.

8. Conclusions

Börzsönyi *et al.* (2009) showed experimentally and with DEM simulations that a dense monodisperse granular flow down an inclined plane can become unstable, forming a series of longitudinal stripes that align with the downslope motion. The instability was found for slope angles ζ in the range $[34°, 39°]$ and had subtly raised denser ridges that flowed downslope faster than the troughs. Superposed on top of this motion was a much weaker secondary flow that slowly transported surface grains from the troughs towards the ridges. This regime differentiated itself from the longitudinal stripes observed by Forterre & Pouliquen (2001, 2002), which occur at higher slope angles and transport surface grains from the ridges to the troughs. Pearse *et al.* (2026) performed experiments in the dense regime of Börzsönyi *et al.* (2009), but with a size-bidisperse mixture of differently coloured particles of the same intrinsic density. Figure 1 shows a deposit formed on a curved chute that transitioned from 46° at its steepest point to 17° at its shallowest point. It has a series of alternating bands of large green and small white particles that also align with the dominant downslope motion. Pearse *et al.* (2026) excavated the deposit to show that the bands of large and small particles visible at the surface, extended all the way through the flow depth. This contrasts strongly with the inversely graded deposit that one might expect.

https://doi.org/10.1017/jfm.2026.12176

Pearse *et al.* (2026) argued that the transversely segregated striped pattern was due to the underlying secondary motion rotating the sharply segregated interface between the large and small particles from being slope parallel to slope normal. Moreover, they showed that a standard particle-size-segregation model (see e.g. Gray 2018) could capture this effect if an underlying secondary flow consisting of a series of counter-rotating vortices was assumed to exist. In the absence of diffusion, the model predicted that at steady state the secondary flow would produce a series of large–rich bands, centred on the downwelling parts of the flow, that were interspersed by a series of small–rich bands, centred on the upwelling regions. In order to allow the large and small particles to recirculate, the large– and small–rich bands were separated by a series of breaking-size-segregation waves that were also aligned with the downslope direction (Thornton & Gray 2008; Gray & Ancey 2009; Gray & Kokelaar 2010*a*,*b*; Edwards *et al.* 2023). This conceptual picture is summarised in figure 2. Each complete stripe (measured from centre to centre of each large–rich band) therefore consists of a pair of counter-rotating vortices.

This paper extends Pearse *et al.*'s (2026) work by including the effect of isotropic diffusion in the segregation equation (2.5). In particular, diffusion competes against the overturning effect of the secondary flow and smooths out the sharp interface between large and small particles that occurs in the absence of diffusion. This leads to a rich solution structure, which is dependent on the ratio of the segregation velocity to the convective velocity Λ and the ratio of the segregation velocity to diffusive velocity Pe, defined in (2.17*a*,*b*). To illustrate this, the segregation-advection-diffusion equation is specialised to the case in which the flow is spatially uniform in the downslope direction (2.10), a secondary flow (2.12)–(2.13) is prescribed, and the equation is non-dimensionalised (2.14) to give the non-dimensional segregation-advection-diffusion equation (2.16). Figure 5 illustrates what happens in a single clockwise rotating secondary vortex over a wide range of parameter space. For sufficiently small Λ and large Pe, steady states form that still have well-defined large– and small–rich bands that extend all the way through the flow depth. However, as Λ increases, the diffusion competes against the overturning effect to produce solutions with wavy interfaces between the large and small particles, and with only large particles visible at the surface. Transversely segregated longitudinal stripes will therefore not be visible at the free surface in this case, even though there is still an underlying secondary flow.

In figure 5, the cases $(Pe, \Lambda) = (500, 100)$ and $(50, 10)$ are particularly interesting, because the wavy interface shapes look similar and are both quite sharp. This suggests that it is possible to derive a depth-averaged segregation model to capture the interface dynamics (see e.g. Gray & Kokelaar 2010*a*,*b*). In § 4 the depth-averaged segregation equation (4.4) is derived, which, importantly, includes the effects of lateral diffusion for the first time. In order to use it, a number of approximations still need to be made to evaluate the integrals in (4.3) as well as in the depth-averaged diffusive terms. This is done first just in the cross-slope direction in § 5 assuming the same flow field as in § 3 and that the flow is of constant height and spatially uniform in the downslope direction. Assuming that the flow is always sharply inversely graded (i.e. all the large particles are on top of all the small ones), the resulting non-dimensional depth-averaged segregation-advection-diffusion equation for the interface height $\tilde{\eta}$ in the cross-slope direction is given in the partial differential equation (5.7). This has certain similarities to the non-depth-averaged segregation-advection-diffusion equation (2.16) and contains the same non-dimensional parameters Pe and Λ. In (2.16), the segregation term has a quadratic flux $\phi^s(1-\phi^s)$ that drives the segregation in the slope-normal direction $\tilde{z}$, and shuts off when $\phi^s = 0$ or 1. While this term no longer appears in the depth-averaged segregation-diffusion equation (5.7), the terms associated with the secondary motion have a similar quadratic flux $\tilde{\eta}^2 - \tilde{\eta}$

https://doi.org/10.1017/jfm.2026.12176

that now seeks to segregate the material in the cross-slope direction $\tilde{y}$, and shuts off when $\tilde{\eta} = 0$ or 1. Since this factor is premultiplied by a sine function, the direction of segregation oscillates periodically in $\tilde{y}$. The depth-averaged segregation-advection-diffusion equation (5.7) therefore has the net effect of driving large particles to the downwelling regions and the small particles to the upwelling regions, as observed in experiments.

Numerical solutions to the depth-averaged segregation-advection-diffusion equation are compared with the non-depth-averaged case in figure 7(*a–e*). For the case $(Pe, \Lambda) = (500, 100)$ the theory almost exactly captures the evolution of the sharp inversely graded interface in space and time. Since the model includes diffusion, it is able to compete against the overturning effect of the secondary recirculation and generates a steady state with a sharp 'S'-shaped profile. In § 5.4 the exact solution (5.13) is derived for the steady-state interface height $\tilde{\eta}$, which depends on the non-dimensional parameter Ξ defined in (5.14). In Ξ, Pe and Λ appear as a ratio. It follows that, for the same width cell, solutions with the same value of Pe/Λ have the same steady-state depth-averaged interface shape. Indeed, this is why the interfaces in the non-depth-averaged solutions look similar for $(Pe, \Lambda) = (500, 100)$ and $(50, 10)$ in figure 5. The only difference between them is that the lower value of Pe has a more diffuse interface in the full two-dimensional solution.

Figure 7(*f–j*) compares the depth-averaged theory with the full solution for the case $(Pe, \Lambda) = (500, 3/2)$, when the secondary recirculation is stronger than the effect of the lateral diffusion. In this case the two solutions are in good agreement at early times, but the lateral diffusion is not strong enough to prevent the interface steepening up to the vertical and overturning to form a breaking-size-segregation wave in the two-dimensional case. At later times, the depth-averaged theory continues to be able to predict the evolution of the interface away from the breaking-size-segregation wave, which is represented as a diffuse shock. While this diffuse shock fails to capture the detailed structure of the breaking wave, it does predict its average lateral position. The depth-averaged theory therefore has the potential to model situations that lie outside the domain for which it was derived. It also has the advantage that it reduces a complicated two-dimensional segregation problem to a relatively simple one-dimensional one. Indeed, in the absence of diffusion, it can be reduced to a quasi-linear problem that can be solved exactly by using the method of characteristics and a shock-fitting procedure, as shown in § 5.5 and figure 8.

The simplified depth-averaged description (4.4) can also be used to solve spatially two-dimensional time-dependent problems, such as the evolution of the stripes down a chute from an inversely graded inflow. The experiments in § 6 show that a white band initially forms adjacent to each sidewall and is flanked by a thinner large–rich band that is adjacent to the central region. This structure becomes fully developed by approximately one metre downstream of the inflow. The central flow on the other hand stays a uniform green colour until approximately 1.2 m downstream when subtle oscillations in concentration develop at the surface, that become progressively stronger with increasing downstream distance. An approximately steady-state particle-size distribution develops 2.3 m downstream and consists of six large–rich longitudinal bands (figure 9 and movie 7). The conceptual model, shown in figure 2, therefore suggests that there should be twelve counter-rotating secondary vortices across the flow. Measurements of the surface velocity (figure 10) show that there are slower moving boundary layers adjacent to each sidewall, and that the central region moves downslope at approximately the same speed, although the large–rich bands move slightly faster than the fines-rich ones. The cross-slope surface velocity is much harder to measure, because it is so much smaller in magnitude compared with the downslope surface velocity. Our attempts to measure v^s did not produce accurate data (not shown), although the results were broadly consistent with the existence of twelve counter-rotating secondary vortices across the channel width.

https://doi.org/10.1017/jfm.2026.12176

In § 7, expressions (7.9) and (7.16) are derived for the down- and cross-slope fluxes, respectively. These take account of the sidewall boundary layers as well as the existence of twelve secondary vortices across the width of the chute. Interestingly, the fluxes in both the x and y directions contain the factor $\eta(\eta - H)$. This acts like a segregation term, and seeks to drive the solution towards a state in which $\eta = 0$ or $\eta = H$. In the absence of secondary flow, the downslope term would normally segregate large particles to the front of the flow and small particles to the rear, as in the segregation-induced fingering problems of Woodhouse *et al.* (2012) and Baker *et al.* (2016). Here, however, the secondary flow is dominant, and segregates the grains within each secondary vortex cell, to create a transversely banded structure that is able to extend all the way through the flow depth (in the absence of diffusion). Once this happens, segregation in the downslope direction shuts off, because within each pure band of large or small particles there is no inversely graded structure that can be sheared through the flow depth, and so large particles are no longer preferentially transported to the flow front.

In § 7.4 the experimental scaling laws of Utter & Behringer (2004) and Trewhela *et al.* (2021) are used to determine realistic approximations for the segregation velocity q and the diffusivity D. In addition, during stripe formation the dominant balance in the depth-averaged segregation equation (7.1) is between the downslope gradient of the downslope flux and the cross-slope gradient of the cross-slope flux. This suggests the scaling law (7.25), which allows the approximate rotational speed of the secondary vortices to be inferred from experiments. With these parameters, the depth-averaged theory is used to solve for the time-dependent formation of the transversely segregated stripes in the channel (see figures 13 and 14, as well as movies 9 and 10). As experimentally observed, the white fines-rich bands first emerge next to the sidewalls and grow in width with increasing downstream distance, until they are fully formed by approximately 1.2 m downstream. At this point the stripes in the centre of the channel also start to emerge, and become progressively stronger with increasing downstream distance, reaching a steady state at approximately 2.3 m downstream. The large–rich and fines-rich bands extend all the way through the flow depth. All these features are in excellent agreement with those observed in experiments in § 6 and in Pearse *et al.* (2026).

The results in this paper demonstrate the power of the simple depth-averaged segregation theory in § 7. In particular, it is able to efficiently solve for the time and spatial development of the stripes down the chute. This could in principle also be done with the non-depth-averaged segregation equation (2.5), but it would involve solving a three-dimensional problem for the small-particle concentration $\phi^s(x, y, z, t)$ rather than a two-dimensional one for the interface height $\eta(x, y, t)$. In both cases, the solutions rely on the formation of a series of counter-rotating secondary vortices that are oriented in the downslope direction.

A key goal for the future must be to understand how and why the secondary vortices form in the first place. This is likely to require the development of new granular constitutive laws that go beyond the $\mu(I)$ rheology (GDR-MiDi 2004; Jop *et al.* 2006; Barker & Gray 2017; Barker *et al.* 2021; Maguire *et al.* 2024; Lloyd *et al.* 2025). In particular, McElwaine *et al.* (2012), Srivastava *et al.* (2021) and Kim & Kamrin (2023) have shown that the incompressible $\mu(I)$-rheology can be extended to include second-normal-stress differences, which are sufficient to drive secondary flows. Indeed, recent experiments, DEM simulations and asymptotic solutions in a (shallow) transversely curved channel, show that the flow bows upwards in the channel centre and forms two counter-rotating vortices that transport material from the sides of the flow along the surface towards the central ridge (Gadal *et al.* 2026). This is consistent with the observations of Börzsönyi *et al.* (2009), and shows promise, but at the moment it is not clear how to

https://doi.org/10.1017/jfm.2026.12176

generalise the theory to the case with no lateral curvature. Krishnaraj & Nott (2016) and Dsouza & Nott (2021) have shown that in very slow flows, secondary motion can also be driven by dilatation, so the full picture may require compressible extensions of the $\mu(I)$-rheology such as those of Barker *et al.* (2017), Heyman *et al.* (2017) and Schaeffer *et al.* (2019). These theories have also been designed to be mathematically well posed, which is something that the original form of the $\mu(I)$-rheology does not guarantee (Barker *et al.* 2015). There is therefore a very rich research area to be explored here, where experiments and DEM simulations can play an important role in narrowing down the key physics that needs to be included in continuum models.

If there are density differences between the particles, or the particle-size ratio is large enough to generate effective density differences (Gamble *et al.* 2026), then the secondary motion can be driven by particle segregation through a Rayleigh–Taylor-like instability (D'Ortona & Thomas 2020; D'Ortona *et al.* 2024; D'Ortona & Thomas 2025). This effect can potentially be captured by coupling either the depth-averaged theory (7.1), or the full segregation equation (2.5), to the bulk dynamics in a similar way to Baker *et al.* (2016), Barker *et al.* (2021) or Maguire *et al.* (2024). However, incorporating the density differences into the bulk rheology is also challenging, and will probably require a compressible granular theory (Schaeffer *et al.* 2019).

While continuum models for the formation of secondary vortices may be some way off, the theory in this paper illustrates how continuum theories can be used to model the segregation in such flows. Although the results are for a highly simplified bidisperse mixture of grains, it would be interesting to investigate whether terrestrial deposits (Shreve 1966; Post 1967; McSaveney 1978; Dufresne & Davies 2009; Magnarini *et al.* 2021*a*, 2024) generate segregated flow bands or wavy interfaces that resemble the structures in figure 5. This would provide further evidence for secondary vortices being the cause of longitudinal ridges in long-runout landslides, and help interpret deposits on Mars (Magnarini *et al.* 2019, 2024) and the Moon (Magnarini *et al.* 2021*b*).

Supplementary movies. Supplementary movies are available at https://doi.org/10.1017/jfm.2026.12176.

Funding. A.P.P. was supported by an Engineering and Physical Sciences Research Council (EPSRC) Doctoral Training Award. C.G.J. and J.M.N.T.G. were supported by Natural Environment Research Council (NERC) grants NE/X00029X/1 and NE/X013936/1. J.M.N.T.G. was also supported by a Royal Society Wolfson Research Merit Award (WM150058) and an EPSRC Established Career Fellowship (EP/M022447/1).

Declaration of interests. The authors report no conflict of interest.

Data availability statement. All research data supporting this publication are directly available within this publication.

References

Abramowitz, M. & Stegun, I. 1970 *Handbook of Mathematical Functions*, 9th edn., p. 11. Dover.

Baker, J., Johnson, C.G. & Gray, J.M.N.T. 2016 Segregation-induced finger formation in granular free-surface flows. *J. Fluid Mech.* **809**, 168–212.

Barker, T. & Gray, J.M.N.T. 2017 Partial regularisation of the incompressible $\mu(I)$-rheology for granular flow. *J. Fluid Mech.* **828**, 5–32.

Barker, T., Rauter, M., Maguire, E.S.F., Johnson, C.G. & Gray, J.M.N.T. 2021 Coupling rheology and segregation in granular flows. *J. Fluid Mech.* **909**, A22.

Barker, T., Schaeffer, D.G., Bohórquez, P. & Gray, J.M.N.T. 2015 Well-posed and ill-posed behaviour of the $\mu(I)$-rheology for granular flows. *J. Fluid Mech.* **779**, 794–818.

Barker, T., Schaeffer, D.G., Shearer, M. & Gray, J.M.N.T. 2017 Well-posed continuum equations for granular flow with compressibility and $\mu(I)$-rheology. *Proc. R. Soc. Lond. A* **473**, 20160846.

Börzsönyi, T., Ecke, R.E. & McElwaine, J.N. 2009 Patterns in flowing sand: understanding the physics of granular flow. *Phys. Rev. Lett.* **103**, 178302.

https://doi.org/10.1017/jfm.2026.12176

BOUZID, M., IZZET, A., TRULSSON, M., CLÉMENT, E., CLAUDIN, P. & ANDREOTTI, B. 2015 Non-local rheology in dense granular flows: revisiting the concept of fluidity. *Eur. Phys. J. E* **38**, 125.

BOUZID, M., TRULSSON, M., CLAUDIN, P., CLÉMENT, E. & ANDREOTTI, B. 2013 Nonlocal rheology of granular flows across yield conditions. *Phys. Rev. Lett.* **111** (23), 238301.

BRODU, N., DELANNAY, R., VALANCE, A. & RICHARD, P. 2013 Shallow granular flows down flat frictional channels: steady flows and longitudinal vortices. *Phys. Rev. E* **87**, 022202.

BRODU, N., DELANNAY, R., VALANCE, A. & RICHARD, P. 2015 New patterns in high-speed granular flows. *J. Fluid Mech.* **769**, 218–228.

CAMPBELL, C.S. 1989 Self-lubrication for long runout landslides. *J. Geol.* **97** (6), 653–665.

CAMPBELL, C.S., CLEARY, P.W. & HOPKINS, M. 1995 Large-scale landslide simulations: global deformation, velocities and basal friction. *J. Geophys. Res.* **100** (B5), 8267–8283.

CHADWICK, P. 1976 *Continuum Mechanics. Concise Theory and Problems*. George Allen & Unwin.

D'ORTONA, U., LUEPTOW, R.M. & THOMAS, N. 2024 Origin of granular axial segregation bands in a rotating tumbler: an interface-mixing driven Rayleigh–Taylor instability. *Phys. Rev. Res.* **6**, L032038.

D'ORTONA, U. & THOMAS, N. 2020 Self-induced Rayleigh–Taylor instability in segregating dry granular flows. *Phys. Rev. Lett.* **124**, 178001.

D'ORTONA, U. & THOMAS, N. 2025 Rayleigh–Taylor instability in two-layer granular flows. *Phys. Rev. E* **112**, 015421.

DSOUZA, P.V. & NOTT, P.R. 2021 Dilatancy-driven secondary flows in dense granular materials. *J. Fluid Mech.* **914**, A36.

DUFRESNE, A. & DAVIES, T.R. 2009 Longitudinal ridges in mass movement deposits. *Geomorphology* **105**, 171–181.

EDWARDS, A.N. & GRAY, J.M.N.T. 2015 Erosion-deposition waves in shallow granular free-surface flows. *J. Fluid Mech.* **762**, 35–67.

EDWARDS, A.N., ROCHA, F.M., KOKELAAR, B.P., JOHNSON, C.G. & GRAY, J.M.N.T. 2023 Particle-size segregation in self-channelised granular flows. *J. Fluid Mech.* **955**, A38.

ESHUIS, P., VAN DER WEELE, K., VAN DER MEER, D. & LOHSE, D. 2005 Granular Leidenfrost effect: experiment and theory of floating particle clusters. *Phys. Rev. Lett.* **95**, 258001.

FORTERRE, Y. & POULIQUEN, O. 2001 Longitudinal vortices in granular flows. *Phys. Rev. Lett.* **86**, 5886.

FORTERRE, Y. & POULIQUEN, O. 2002 Stability analysis of rapid granular chute flows: formation of longitudinal vortices. *J. Fluid Mech.* **467**, 361–387.

GADAL, C., JOHNSON, C.G. & GRAY, J.M.N.T. 2026 Surface curvature and secondary vortices in steady dense shallow granular flows. *J. Fluid Mech.* **1027**, A34.

GAMBLE, P.G., WEBB, J.P., GRAY, J.M.N.T. & JOHNSON, C.G. 2026 Reversed, suppressed and layered granular segregation at large particle size ratios. *J. Fluid Mech.* **1030**, A58.

GDR-MiDi 2004 On dense granular flows. *Eur. Phys. J. E* **14**, 341–365.

GOLDHIRSCH, I. 2003 Rapid granular flows. *Annu. Rev. Fluid Mech.* **35**, 267–293.

GRAY, J.M.N.T. 2018 Particle segregation in dense granular flows. *Annu. Rev. Fluid Mech.* **50**, 407–433.

GRAY, J.M.N.T. & ANCEY, C. 2009 Segregation, recirculation and deposition of coarse particles near two-dimensional avalanche fronts. *J. Fluid Mech.* **629**, 387–423.

GRAY, J.M.N.T. & ANCEY, C. 2011 Multi-component particle size-segregation in shallow granular avalanches. *J. Fluid Mech.* **678**, 535–588.

GRAY, J.M.N.T. & CHUGUNOV, V.A. 2006 Particle-size segregation and diffusive remixing in shallow granular avalanches. *J. Fluid Mech.* **569**, 365–398.

GRAY, J.M.N.T. & KOKELAAR, B.P. 2010*a* Large particle segregation, transport and accumulation in granular free-surface flows. *J. Fluid Mech.* **652**, 105–137.

GRAY, J.M.N.T. & KOKELAAR, B.P. 2010*b* Large particle segregation, transport and accumulation in granular free-surface flows—ERRATUM. *J. Fluid Mech.* **657**, 539.

GRAY, J.M.N.T., TAI, Y.C. & NOELLE, S. 2003 Shock waves, dead-zones and particle-free regions in rapid granular free-surface flows. *J. Fluid Mech.* **491**, 161–181.

GRAY, J.M.N.T. & THORNTON, A.R. 2005 A theory for particle size segregation in shallow granular free-surface flows. *Proc. R. Soc. Lond. A* **461**, 1447–1473.

HEYMAN, J., DELANNAY, R., TABUTEAU, H. & VALANCE, A. 2017 Compressibility regularizes the $\mu(I)$-rheology for dense granular flows. *J. Fluid Mech.* **830**, 553–568.

JENKINS, J.T. & SAVAGE, S.B. 1983 A theory for the rapid flow of identical, smooth, nearly elastic, spherical particles. *J. Fluid Mech.* **130**, 187–202.

JOP, P., FORTERRE, Y. & POULIQUEN, O. 2006 A constitutive relation for dense granular flows. *Nature* **441**, 727–730.

https://doi.org/10.1017/jfm.2026.12176

KAMRIN, K. & HENANN, D.L. 2015 Nonlocal modeling of granular flows down inclines. *Soft Matt.* **11**, 179–185.
KAMRIN, K. & KOVAL, G. 2012 Nonlocal constitutive relation for steady granular flow. *Phys. Rev. Lett.* **108** (17), 178301.
KIM, S. & KAMRIN, K. 2023 A second-order non-local model for granular flows. *Frontiers Phys.* **11**, 1092233.
KRISHNARAJ, K.P. & NOTT, P.R. 2016 A dilation-driven vortex flow in sheared granular materials explains a rheometric anomaly. *Nat. Commun.* **7** (1), 10630.
KURGANOV, A. & TADMOR, E. 2000 New high-resolution central schemes for nonlinear conservation laws and convection-diffusion equations. *J. Comput. Phys.* **160**, 241–282.
LEVAY, S., CLAUDIN, P., SOMFAI, E. & BÖRZSÖNYI, T. 2025 Transverse vortices induced by modulated granular shear flows of elongated particles. *Phys. Rev. E* **112**, 015402.
LLOYD, H.A., MAGUIRE, E.S.F., MISTRY, D., REYNOLDS, G.K., JOHNSON, C.G. & GRAY, J.M.N.T. 2025 On the formation of super-stable granular heaps. *J. Fluid Mech.* **1002**, A27.
MAGNARINI, G., CHAMPAGNE, A., MORINO, C., BECK, C., PHILIPPE, M., DECAULNE, A. & CONWAY, S.J. 2024 Long-runout landslides with associated longitudinal ridges in Iceland as analogues of Martian landslide deposits. *Earth Surf. Dyn.* **12**, 657–678.
MAGNARINI, G., MITCHELL, T.M., GOREN, L., GRINDROD, P.M. & BROWNING, J. 2021*a* Implications of longitudinal ridges for the mechanics of ice-free long runout landslides. *Earth Planet. Sci. Lett.* **574**, 117177.
MAGNARINI, G., MITCHELL, T.M., GRINDROD, P.M., GOREN, L. & SCHMITT, H.H. 2019 Longitudinal ridges imparted by high-speed granular flow mechanisms in martian landslides. *Nat. Commun.* **10**, 4711.
MAGNARINI, G., MITCHELL, T.M., GRINDROD, P.M., SCHMITT, H.H. & PETRO, N.E. 2021*b* Scaling relationship between the wavelength of longitudinal ridges and the thickness of long runout landslides on the Moon. *J. Geophys. Res.: Planets* **126**, e2021JE006922.
MAGUIRE, E.S.F., BARKER, T., RAUTER, M., JOHNSON, C.G. & GRAY, J.M.N.T. 2024 Particle-size segregation patterns in a partially filled triangular rotating drum. *J. Fluid Mech.* **979**, A40.
MCELWAINE, J.N., TAKAGI, D. & HUPPERT, H.E. 2012 Surface curvature of steady granular flows. *Granul. Matt.* **14**, 229–234.
MCSAVENEY, M.J. 1978 Chapter 6 - Sherman glacier rock avalanche, Alaska, U.S.A.. In *Rockslides and Avalanches, 1* (ed. B. Voight), vol. 14, pp. 197–258. Elsevier.
MEDOVIKOV, A.A. 1998 High order explicit methods for parabolic equations. *BIT* **38** (2), 372–390.
PEARSE, A.P., JOHNSON, C.G. & GRAY, J.M.N.T. 2026 Longitudinal stripe formation in bidisperse granular free-surface avalanches with secondary vortices. *J. Fluid Mech.* **1032**, A4.
POST, A. 1967 Effects of the March 1964 Alaska earthquake on glaciers. U.S. Geological Survey Professional Paper 544-D, pp. D1–D42.
POULIQUEN, O. 1999 On the shape of granular fronts down rough inclined planes. *Phys. Fluids* **11** (7), 1956–1958.
POULIQUEN, O., DELOUR, J. & SAVAGE, S.B. 1997 Fingering in granular flows. *Nature* **386**, 816–817.
ROCHA, F.M., JOHNSON, C.G. & GRAY, J.M.N.T. 2019 Self-channelization and levee formation in monodisperse granular flows. *J. Fluid Mech.* **876**, 591–641.
SAVAGE, S.B. & HUTTER, K. 1989 The motion of a finite mass of granular material down a rough incline. *J. Fluid Mech.* **199**, 177–215.
SAVAGE, S.B. & LUN, C.K.K. 1988 Particle size segregation in inclined chute flow of dry cohesionless granular solids. *J. Fluid Mech.* **189**, 311–335.
SCHAEFFER, D.G., BARKER, T., TSUJI, D., GREMAUD, P., SHEARER, M. & GRAY, J.M.N.T. 2019 Constitutive relations for compressible granular flow in the inertial regime. *J. Fluid Mech.* **874**, 926–951.
SHREVE, R.L. 1966 Sherman landslide, Alaska. *Science* **154**, 1639–1643.
SRIVASTAVA, I., SILBERT, L.E., GREST, G.S. & LECHMAN, J.B. 2021 Viscometric flow of dense granular materials under controlled pressure and shear stress. *J. Fluid Mech.* **907**, A18.
TABERLET, N., RICHARD, P. & DELANNAY, R. 2009 Leidenfrost granular flows. In *Traffic and Granular Flow '07* (ed. C. Appert-Rolland, F. Chevoir, P. Gondret, S. Lassarre, J.-P. Lebacque & M. Schreckenberg), pp. 565–576. Springer Berlin Heidelberg.
THIELICKE, W. & STAMHUIS, E.J. 2014 PIVLab – towards user-friendly, affordable and accurate digital particle image velocimetry in MATLAB. *J. Open Res. Softw.* **2**, e30.
THORNTON, A.R. & GRAY, J.M.N.T. 2008 Breaking size-segregation waves and particle recirculation in granular avalanches. *J. Fluid Mech.* **596**, 261–284.
TREWHELA, T., ANCEY, C. & GRAY, J.M.N.T. 2021 An experimental scaling law for particle-size segregation in dense granular flows. *J. Fluid Mech.* **916**, A55.
UTTER, B. & BEHRINGER, R.P. 2004 Self-diffusion in dense granular shear flows. *Phys. Rev. E* **69**, 031308.

https://doi.org/10.1017/jfm.2026.12176

VIROULET, S., BAKER, J.L., ROCHA, F.M., JOHNSON, C.G. & GRAY, J.M.N.T. 2018 The kinematics of bidisperse granular roll waves. *J. Fluid Mech.* **848**, 836–875.

WANG, T., JING, L., KWOK, C.Y., SOBRAL, Y.D., WEINHART, T. & THORNTON, A.R. 2025 Basal layer of granular flow down smooth and rough inclines: kinematics, slip laws and rheology. *J. Fluid Mech.* **1025**, A27.

WHITHAM, G.B. 1974 *Linear and Nonlinear Waves*. John Wiley.

WOODHOUSE, M.J., THORNTON, A.R., JOHNSON, C.G., KOKELAAR, B.P. & GRAY, J.M.N.T. 2012 Segregation-induced fingering instabilities in granular free-surface flows. *J. Fluid Mech.* **709**, 543–580.

https://doi.org/10.1017/jfm.2026.12176